The impact of electrogenic sulfide oxidation on elemental cycling and solute fluxes in coastal sediment

Alexandra M.F. Rao [a,*], Sairah Y. Malkin [a,1], Silvia Hidalgo-Martinez [b], Filip J.R. Meysman [b,a]

[a] *Department of Analytical, Environmental and Geochemistry, Vrije Universiteit Brussel, Pleinlaan 2, 1050 Brussels, Belgium*
[b] *Department of Ecosystem Studies, Royal Netherlands Institute for Sea Research, Korringaweg 7, 4401 NT Yerseke, The Netherlands*

Abstract

Filamentous sulfide oxidizing cable bacteria are capable of linking the oxidation of free sulfide in deep anoxic layers of marine sediments to the reduction of oxygen or nitrate in surface sediments by conducting electrons over centimeter-scale distances. Previous studies have shown that this newly discovered microbial process, referred to as electrogenic sulfide oxidation (e-SOx), may alter elemental cycling in sediments, but the nature and rates of the resulting biogeochemical transformations and their influence on benthic-pelagic coupling remain largely unknown. Here we quantify changes in sediment geochemistry and solute fluxes at the sediment–water interface as e-SOx develops and declines over time in laboratory incubations of organic-rich sediments from a seasonally hypoxic coastal basin (Marine Lake Grevelingen, The Netherlands).

Our results show that e-SOx enhanced sediment O_2 consumption and acidified subsurface sediment, resulting in the dissolution of calcium carbonate and iron sulfide minerals in deeper sediment horizons and the associated accumulation of dissolved iron, manganese, and calcium in porewater. Remobilized Fe diffusing upward was reoxidized at the sediment–water interface, producing an amorphous Fe oxide crust, while dissolved Fe diffusing downward was reprecipitated in the form of FeS as it encountered the free sulfide horizon. The development of e-SOx enhanced the diffusive release of dissolved Mn at the sediment–water interface, capped the phosphate efflux, generated a buildup of organic matter in surface sediments, and strongly stimulated the release of alkalinity from the sediment. About 75% of this alkalinity production was associated with net $CaCO_3$ dissolution, while the remaining 25% was attributed to a pumping mechanism that transfers alkalinity from anodic H_2S oxidation (an alkalinity sink) in deeper sediments to cathodic O_2 reduction (an alkalinity source) near the sediment–water interface. The resulting sediment alkalinity efflux buffers the release of dissolved inorganic carbon at the sediment–water interface, and may therefore counteract the influence of benthic respiration on coastal ocean pH. Overall, our results demonstrate that e-SOx development strongly affects the biogeochemical cycles of C, P, Ca, Fe, Mn, and S in coastal sediments.

---

* Corresponding author at: Université du Québec à Rimouski, Institut des Sciences de la Mer, 310 Allée des Ursulines, Rimouski, QC, Canada.
E-mail address: alexandra_rao@uqar.ca (A.M.F. Rao).
[1] Current address: Horn Point Laboratory, University of Maryland Center for Environmental Science, Cambridge, MD 21613, USA.

1. INTRODUCTION

In recent years, it has been shown that filamentous cable bacteria carry out long-distance electron transport and thereby couple spatially separated redox half-reactions over centimeter-scale distances in marine sediment (Nielsen et al., 2010; Pfeffer et al., 2012). The evidence for

long-distance electron transport was originally inferred from a characteristic set of O_2, pH and H_2S profiles in the sediment, but recently, further support for this process has been obtained by high-resolution profiling of electric potential in sediments (Damgaard et al., 2014), which reveals the predicted electric field (Risgaard-Petersen et al., 2014). Long-distance electron transport is induced by a novel microbial process, termed electrogenic sulfide oxidation (e-SOx), in which free sulfide is removed down to 2–3 cm depth in sediments by anodic sulfide oxidation ($\frac{1}{2}H_2S + 2H_2O \rightarrow \frac{1}{2}SO_4^{2-} + 4e^- + 5H^+$), while O_2 consumption in oxic surface sediments is enhanced by cathodic O_2 reduction ($O_2 + 4e^- + 4H^+ \rightarrow 2H_2O$), reducing the O_2 penetration depth. Electrogenic sulfide oxidation is therefore capable of creating a thick suboxic zone in sediments where both oxygen and sulfide are below detection. Pfeffer et al. (2012) suggested that electrons are passed from cell to cell along the longitudinal axis of cable bacteria filaments, based on targeted perturbation experiments in which the electrical current was short-circuited by passing a thin wire through the sediment, observations of morphological properties using light, atomic force, transmission electron and scanning electron microscopy, and observations of conductive properties using electrostatic force microscopy.

The spatial separation of oxidation and reduction half-reactions implies a corresponding separation in proton production and consumption, resulting in a distinctive porewater pH distribution in sediments. A sharp pH maximum occurs near the O_2 penetration depth due to proton consumption by cathodic O_2 reduction, while acidic conditions are observed at the bottom of the suboxic zone due to proton release by anodic sulfide oxidation (Nielsen et al., 2010). This porewater pH signature, in combination with shallow O_2 penetration and a thick suboxic zone in sediments represent a reliable indicator of e-SOx activity (Meysman et al., 2015). In a pioneering study, Risgaard-Petersen et al. (2012) demonstrated that the impact of e-SOx on porewater pH can strongly alter elemental cycling in laboratory sediment incubations. The low pH in suboxic sediments stimulates the dissolution of carbonate and iron sulfide minerals. Mobilized Fe^{2+} and Ca^{2+} subsequently diffuse upward and are redeposited as high Mg calcite and Fe oxide minerals in oxic surface sediments.

As e-SOx alters sediment biogeochemistry in laboratory incubations, it is conceivable that this process may play an important role in elemental cycling in coastal environments, where the water column is shallow and an important part of ecosystem metabolism takes place in the sediment (Heip et al., 1995). For example, Rao et al. (2014) have suggested that e-SOx development may enhance alkalinity generation in coastal sediments, based on incubations of defaunated sands. Benthic alkalinity production may offset the effect of dissolved inorganic carbon (DIC) production by benthic respiration on the acidification of coastal waters, and favor the uptake of atmospheric CO_2 (Thomas et al., 2009; Hu and Cai, 2011). This observation has sparked great interest in quantifying the rates and mechanisms of alkalinity production in coastal sediments (Faber et al., 2012; Rao et al., 2012, 2014; Cyronak et al., 2013a,b). To date, these studies have focused on three known sources of alkalinity

in coastal sediments: (1) denitrification, (2) the anaerobic oxidation of organic matter by iron and sulfate reduction followed by the accumulation of reduced iron sulfide minerals, and (3) the dissolution of sedimentary carbonate, favored by the production of metabolic acidity including respiratory CO_2. In this study, we investigated the hypothesis that e-SOx represents an additional, and presently overlooked pathway of alkalinity generation in coastal sediments by stimulating net carbonate dissolution and reversing FeS accumulation.

While e-SOx was first discovered in laboratory experiments (Nielsen et al., 2010), it has recently been observed in a range of natural environments including coastal mud plains, aquaculture areas, salt marshes, and seasonally hypoxic basins (Malkin et al., 2014). Nevertheless, the controls on the natural spatial and temporal distribution of e-SOx in coastal sediments and its role in benthic-pelagic coupling in coastal ecosystems remain unclear. The goal of the present study was to examine the influence of e-SOx on elemental cycling and solute exchange at the sediment–water interface, with particular emphasis on alkalinity generation. Building upon previous work by Risgaard-Petersen et al. (2012), we conducted *ex situ* incubations of coastal sediments in which we tracked the wax and wane of e-SOx and quantified the response of carbon, nutrient, metal and sulfur cycling.

2. MATERIALS AND METHODS

2.1. Sediment sampling

Sediments were collected with a box corer aboard the R/V Luctor, at 34 m water depth in Den Osse basin (51°44.834′N, 03°53.401′E, Fig. 1) in Lake Grevelingen, a euhaline coastal marine reservoir (area 108 km², mean water depth 5.3 m; Kelderman et al., 1984) that was formed by the enclosure of a former estuary in the Rhine-Meuse-Scheldt delta area of The Netherlands. Fine-grained, organic rich sediments have accumulated since the Grevelingen was closed off from riverine inputs in 1964 and from the North Sea in 1971. These deposits now form the top ∼100 cm layer of sediments at the sampling station. Sampling took place on 23 April 2012, prior to the development of vernal water column stratification, which is known to cause seasonal hypoxia and anoxia in the deeper basins of Lake Grevelingen. Additional hydrographic information at the time of sampling is provided in Hagens et al. (2015). A previous study has confirmed the natural presence of cable bacteria and associated e-SOx activity in the sediments of Den Osse basin (Malkin et al., 2014).

2.2. Sediment core incubations

Sediments were brought to the Royal Netherlands Institute for Sea Research (NIOZ, Yerseke, The Netherlands), homogenized, and repacked into PMMA coreliners, 15 cm inner diameter and 35 cm in length, for *ex situ* core incubations. All cores contained about 20 cm of sediment and 15 cm of overlying water. Cores were then left to settle for 10 days prior to the start of the experiment (time T0) in
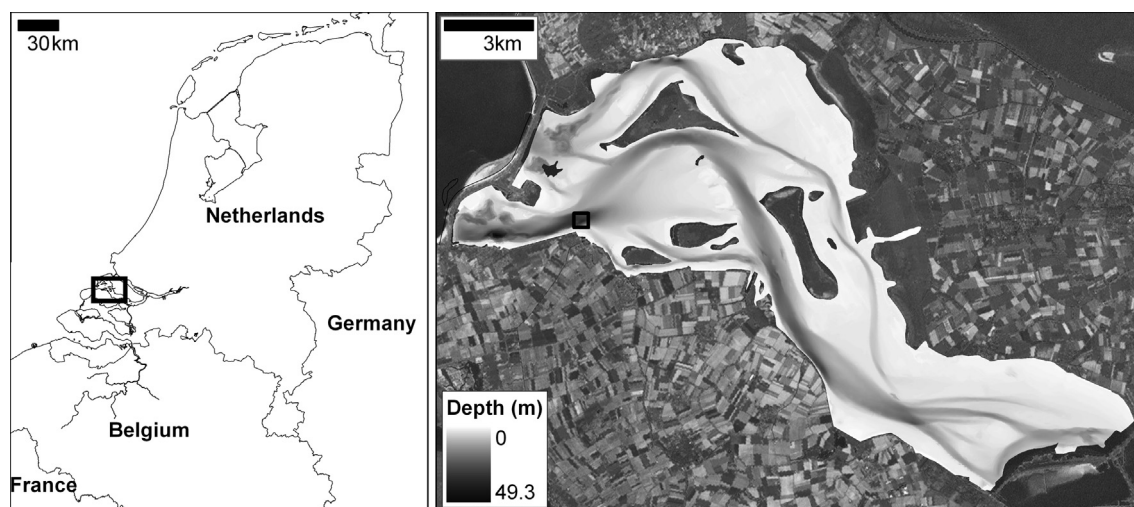
Fig. 1. Location of sediment sampling for incubations.

a darkened water bath kept in a temperature-controlled room at 16 °C and continuously aerated. The water in the bath was replaced daily with Oosterschelde seawater, which has a salinity (~30) similar to that observed in Lake Grevelingen. Of thirteen cores, eleven were left in the bath with no lid, allowing a free exchange of the overlying water with the reservoir (oxic treatment), while two cores where closed off with gas-tight lids (anoxic treatment). The latter represent a control treatment, as the absence of O_2 precludes the development of cable bacteria (Nielsen et al., 2010). The impact of the development and decline of e-SOx on interfacial solute fluxes was examined by repeated flux measurements at five time points in oxic cores. No flux measurements were performed on anoxic control cores. The impact of e-SOx on elemental cycling was further studied by comparing porewater microelectrode profiles in oxic and anoxic cores at all five time points, and distributions of porewater and solid phase geochemistry from profiles of discrete samples in oxic cores at these five time points and in anoxic cores at the last time point.

Sampling for porewater solute and solid phase distributions and interfacial solute flux measurements was conducted at five time points: May 7–9 (T0), May 14–16 (T7), May 21–23 (T14), June 11–13 (T35), and July 17–19 (T71). Each time point involved a three day sampling procedure, which was executed in a similar manner. On the first day, microsensor profiles were measured in the two anoxic cores (pH and H_2S only) and three randomly selected oxic cores (O_2, pH and H_2S), with $n = 2$–4 replicate profiles per solute per core, as described in Section 2.4. On the second day, solute fluxes were determined in the three oxic cores used for microsensor profiling on the previous day, as described in Section 2.3. On the third day, two of the same oxic cores were destructively sampled by extracting 3–4 replicate subcores (4 cm i.d.), which were then used for porewater and solid phase analyses as described in Section 2.5. On the fourth day of the final sampling period (T71), the two anoxic control cores were destructively sampled for porewater and solid phase analyses. For both

oxic and anoxic treatments, subcores were extruded and sliced in an anaerobic glove box at 3 mm intervals from 0 to 3 cm, 5 mm intervals from 3 to 5 cm, and 1 cm intervals from 5 to 10 cm depth. Corresponding depth sections from replicate subcores were pooled in centrifuge tubes and centrifuged at 5000 rpm for 5 min. After centrifugation, centrifuge tubes were opened one at a time in the glove box and porewater was dispensed through syringe filters (0.22 μm PVDF) into dedicated sample vials. The remaining sediment was stored frozen (-20 °C) under anoxic conditions for solid phase analyses.

2.3. Solute flux measurements

Solute fluxes across the sediment–water interface were determined in closed core incubations as described in Rao et al. (2014). Briefly, each core was closed with a gas-tight lid containing two sampling ports and a central stirrer, which ensured that the overlying water was well mixed during incubation. An oxygen optode (Presens O_2 dipping probe or Pyroscience robust O_2 probe OXROB10) was pre-calibrated with seawater at 0% and 100% saturation, and inserted in each lid for measurements of total O_2 uptake (TOU, the O_2 flux at the sediment–water interface). A known volume of a sodium bromide (NaBr) tracer solution of the same density as the seawater used in this experiment was added to the core overlying water at the start of each incubation, to a final concentration of 3–4 mmol L^{-1}. Samples of ~30 mL of overlying water were collected from each core in plastic syringes at five time points at approximately hourly intervals for analysis of dissolved inorganic nutrients ($\sum NO_x = NO_3^- + NO_2^-$, Si $(OH)_4$, PO_4^{3-}, NH_4^+), pH, total alkalinity (TA), calcium (Ca^{2+}) and bromide (Br^-), as described in Section 2.5.

The effective volume of overlying water (V_{ow}) was calculated from the known volume (V_{spike}) and concentration (C_{spike}) of Br^- spike solution injected at the start of incubations as $V_{ow} = V_{spike}C_{spike}/C_{ow}^0$. The initial Br^- concentration in excess of natural seawater (C_{ow}^0) was obtained by

extrapolating the measured excess Br^- concentration in the overlying water to the start of the incubation using linear regression (Berelson et al., 1999; Jahnke and Jahnke, 2000).

Solute fluxes (J) across the sediment–water interface were determined based on V_{ow}, the known core cross-sectional area (A), and the slope of a linear regression of overlying water concentration vs. incubation time, as $J = (\Delta C_{ow}/\Delta t)(V_{ow}/A)$. Solute fluxes were corrected for the dilution of overlying water with fresh seawater at each sampling time. As a result of undiluted tracer solution remaining in the injection port, initial Br^-, TA and Ca^{2+} measurements were often anomalous and were not included in the final analysis.

2.4. Microsensor profiling

Porewater microprofiles of O_2, pH and H_2S were measured at a resolution of 200 μm or less, using commercial microelectrodes (pH: 100-μm tip diameter; O_2 and H_2S: 50-μm tip diameter; Unisense A.S., Denmark) operated with a motorized micromanipulator and multimeter (Unisense A.S., Denmark). Oxygen microelectrodes were calibrated in air-saturated seawater (100% saturation) and in anoxic sediment (0% saturation). pH calibrations were made with three NBS standards and a TRIS buffer to correct for salinity effects (Dickson et al., 2007), and pH is reported on the total scale. For H_2S, a 5-point calibration was made using Na_2S standards in acidified seawater (pH < 4), which were kept in an anaerobic glove box and verified by iodometric titration. ΣH_2S was calculated from H_2S based on pH measured at the same depth using the R package CRAN: AquaEnv (Hofmann et al., 2010), with the relations of Millero (1995) for the thermodynamic equilibrium constants of hydrogen sulfide.

Cathodic proton consumption by e-SOx was first calculated as $J_{TA}^{up} - J_{TA}^{down}$, the sum of upward and downward TA fluxes above and below the pH peak at the bottom of the oxic zone, based on the major components of alkalinity (Malkin et al., 2014). Diffusive fluxes of individual component solutes were calculated from solute profiles using Fick's first law, $J = -\phi D \partial C/\partial z$, where z is depth, ϕ porosity, and $\partial C/\partial z$ the concentration gradient. The molecular diffusion coefficient (D^0) was calculated at measured salinity and temperature using the R package CRAN: marelac (Soetaert et al., 2010), and corrected for sediment tortuosity ($D = D^0/\theta^2$) according to: $\theta^2 = 1 - 2 \ln \phi$ (Boudreau, 1997). Concentration gradients for individual solutes were calculated from pH and H_2S microprofiles, TA and nutrient profiles interpolated at a vertical resolution equivalent to the measured microprofile resolution, using the R packages CRAN: AquaEnv (Hofmann et al., 2010) and CRAN: akima (Gebhardt et al., 2009) and assuming constant total borate. Calculated cathodic proton consumption was not corrected for other reactions taking place in the oxic zone, such as nitrification, calcification, and iron oxidation. Since these processes would result in TA consumption, we consider our estimates of cathodic proton consumption to be conservative. Cathodic O_2 reduction was calculated as $0.25\times$ the rate of cathodic proton consumption, which accounts for the consumption of 4 protons per O_2 molecule.

Vasquez-Cardenas et al. (2015) recently reported that the alkalinity balance method above can substantially underestimate cathodic O_2 reduction, which these authors determined as the measured change in TOU upon the disruption of electrogenic metabolism in a targeted manipulation experiment. These findings corroborate an earlier observation by Risgaard-Petersen et al. (2014) that cathodic O_2 reduction calculations based on a proton-oxygen mass balance, as described above, underestimate pH buffering reactions in the oxic zone and pH microprofiles may underestimate the steepness of pH gradients produced by e-SOx. Therefore for comparison, we also calculated cathodic O_2 reduction as TOU (t) – TOU ($t = 0$) following Vasquez-Cardenas et al. (2015), assuming that all changes in TOU during the experiment are attributed to cathodic O_2 reduction. Note that these estimates may slightly overestimate cathodic O_2 reduction, in that they ignore changes in TOU due to the oxidation of upward diffusing NH_4^+, Fe^{2+} and Mn^{2+}.

Electric current density, $J_{current}$, was then calculated as $(1/F) \times$ the rate of cathodic proton consumption, where $F = 96,485$ C mol^{-1} is Faraday's number. The electric field, E, was calculated from $J_{current}$ using Ohm's law, i.e., $E = J_{current}/\sigma_{sed}$, where σ_{sed} represents the effective conductivity of the sediment. The sediment conductivity was calculated as $\sigma_{sed} = \phi \sigma_{PW}/\theta^2$, where σ_{PW} is the conductivity of the porewater.

2.5. Analytical methods

Sediment samples were freeze-dried and ground to a fine powder for analysis of total carbon, total organic carbon (C ± 0.16%), and nitrogen (N ± 0.02%) on a Thermo Scientific Delta V Elemental Analyzer. Samples analyzed for total organic C were first acidified with 0.1 N HCl to remove inorganic C. Total inorganic C was then calculated by difference. Porosity was determined on two separate cores at T0 by drying sediment samples to a constant weight at 60 °C and correcting for the salt content of the porewater.

Overlying water samples for solute flux measurements (Section 2.3) were analyzed immediately upon collection for pH using an Orion ROSS glass electrode calibrated with NBS buffers and a seawater TRIS buffer prepared according to Dickson et al. (2007). Samples for Br^-, Ca^{2+}, TA, and nutrients were filtered (0.2 μm) and refrigerated until analysis. Br^- (±1.2%) was analyzed colorimetrically according to Presley (1971), TA (±0.2%) by Gran titration and Ca^{2+} (±0.05%) by ethylene glycol tetraacetic acid (EGTA) titration (Tsunogai et al., 1968) on acidified samples (10 μL of 6 N HCl per 1 mL sample). Analyses for TA and Ca^{2+} were performed using manual, scaled-down titrations with an ultraprecision micrometer burette (Roger Gilmont Instruments). Replicate measurements of certified reference materials provided by Dickson et al. (2003) and IAPSO standard were used to validate the accuracy of TA and Ca^{2+} measurements. Dissolved inorganic carbon (DIC) in the overlying water was calculated from pH and TA accounting for contributions from borate and nutrients at measured values of salinity and temperature with the R

package CRAN: seacarb (Lavigne et al., 2011), using the relations of Lueker et al. (2000) for the dissociation constants of carbonic acid, Perez and Fraga (1987) for the dissociation constant of hydrogen fluoride, and Dickson (1990) for the dissociation constant of hydrogen sulfate. Calculated DIC concentrations in the overlying water of core incubations were used to determine the DIC flux, J_{DIC}, as described in Section 2.3. The DIC production due to organic matter remineralization was determined by subtracting the net $CaCO_3$ dissolution rate based on J_{Ca} from the DIC flux ($R_{min} = J_{DIC} - J_{Ca}$).

Porewater samples were filtered (0.2 μM) and refrigerated prior to analysis for TA (±0.3%) as described above for overlying water samples. Acidified porewater samples (10 μL of 6 N HCl per 1 mL sample) were analyzed for total dissolved iron ($Fe_d \pm 1.1\%$) using a scaled-down ferrozine method (Viollier et al., 2000), total dissolved manganese ($Mn_d \pm 5\%$) using a scaled-down formaldoxime method corrected for Fe interference (Brewer and Spencer, 1971), sulfate ($SO_4^{2-} \pm 1.1\%$) using the methylthymol blue method (Merks and Sinke, 1981), and Ca^{2+} (±0.1%) on a Perkin–Elmer ICP-OES. Phosphate ($PO_4^{3-} \pm 3.5\%$), silicate ($Si(OH)_4 \pm 0.6\%$), nitrate ($NO_3^- \pm 4.0\%$), nitrite ($NO_2^- \pm 1.7\%$) and ammonium ($NH_4^+ \pm 2.3\%$) concentrations were measured in porewater and overlying water samples using standard colorimetric methods on a Seal QuAAtro autoanalyzer. NO_3^- and NO_2^- analyses were performed on all overlying water samples and T0 porewater samples only (data not shown).

The production and consumption rates of solutes measured in discrete porewater samples were determined from the average of profiles measured in duplicate cores using the program PROFILE (Berg et al., 1998). PROFILE was also used to derive diffusive interfacial fluxes from discrete porewater profiles, with the exception of TA, for which interfacial fluxes were calculated as described in Section 2.4. The removal of fixed nitrogen in sediments was estimated according to $N_r = (R_{min}/r_{C:N}) - J_{DIN}$, where J_{DIN} represents the total flux of dissolved inorganic nitrogen ($DIN = NO_3^- + NO_2^- + NH_4^+$) at the sediment–water interface and $r_{C:N}$ is the mean bulk sediment C:N ratio. Positive N_r denotes nitrogen removal.

For solid phase analyses, frozen sediments were first thawed and homogenized with a spatula. Water content in sediment samples was determined as described above for porosity, and used to correct solid phase analysis results to a dry weight basis. Acid-volatile sulfide ($AVS = H_2S + FeS$) and chromium reducible sulfur (CRS) including elemental sulfur (S^0) and pyrite (FeS_2) were determined using a cold two-step distillation procedure (Kallmeyer et al., 2004). Wet sediment (0.05–0.1 g) was weighed directly into digestion flasks, which were subsequently purged with N_2 gas. After addition of 10 mL of a 6 N HCl solution sparged with N_2, AVS was liberated as H_2S, which was then stripped from solution during 40 min using N_2 as a carrier gas, and collected in a trap containing 10 mL 5% zinc acetate (ZnAc), with a drop of antifoam. We expect that H_2S from amorphous FeS and mackinawite and about 60% of sulfur from greigite are liberated with this cold 6 N HCl extraction procedure (Cornwell and Morse, 1987). The

ZnAc trap was replaced with a fresh trap, and CRS was subsequently determined in the remaining slurry. Following the addition of 20 mL of N,N dimethylformamide (DMF) and 12 mL of a Cr^{2+} solution in 0.5 N HCl, CRS was stripped from the sediment slurry for 40 min using N_2 as a carrier gas, and precipitated in the ZnAc trap. This procedure liberates sulfur from pyrite (FeS_2) and elemental sulfur (S^0), as well as up to 40% of H_2S from greigite remaining after the AVS extraction (Kallmeyer et al., 2004). Sulfide in individual ZnAc traps was measured following the method of Cline (1969) with a Na_2S standard calibrated by iodometric titration.

For S^0 analysis, wet sediment (1–2 g) was weighed into 3 mL of a 20% ZnAc solution, shaken and centrifuged prior to discarding the excess Zn solution. The remaining sediment was shaken overnight with 10 mL of methanol. The samples were then centrifuged, and the methanol supernatant was analyzed for S^0 by HPLC (Thamdrup and Canfield, 1996).

Ascorbate and dithionite extractions were used for the analysis of solid phase Fe. For ascorbate extractions, wet sediment (0.1–0.5 g) was weighed directly into centrifuge tubes with 10 mL of an extractant solution containing 10 g of trisodium citrate dihydrate and 10 g sodium bicarbonate in 200 mL of deionized water, which was purged with N_2 prior to the addition of 5 g of ascorbic acid. Samples were shaken for 2 h at room temperature. Kostka and Luther (1994) demonstrated that this procedure extracts amorphous Fe oxides nearly quantitatively, and liberates about 30% of FeS.

For dithionite extractions, wet sediment (0.1–0.5 g) was weighed into centrifuge tubes, to which 10 mL of an extractant solution containing 2 mL glacial acetic acid and 5.9 g trisodium citrate dihydrate in 100 mL of deionized water, and 0.5 g of sodium dithionite was added. Samples were shaken for 4 h at 60 °C. This procedure liberates total reactive Fe, including amorphous and crystalline Fe oxides, AVS, and Fe silicates which may be amorphous (Kostka and Luther, 1994). Dissolved iron in ascorbate (Fe_{ASC}) and dithionite (Fe_{DCA}) extracts was measured as described above for acidified porewater samples.

The total inventory I of solid phase compounds was calculated as:

$$I = \int_0^L [1 - \phi(x)] \frac{\rho_s}{M_i} C_i(x) dx \tag{1}$$

where $\phi(x)$ is the porosity profile, M_i the molecular weight, $C_i(x)$ the solid phase concentration (g per g dry sediment), L the sediment depth over which the inventory is calculated, and assuming the solid phase density of quartz ($\rho_s = 2.65$ g cm^{-3}).

2.6. Fluorescence in situ hybridisation

The presence of cable bacteria was verified by fluorescence in situ hybridisation (FISH) according to Schauer et al. (2014) with probe DSB706 (Manz et al., 1992), on sediment at 2.1–2.4 cm depth in 2 oxic cores sampled at T14, and at 2.7–3 cm depth in 2 oxic cores sampled at T35. Sediment was frozen at -20 °C prior to analysis.

2.7. Statistical analyses

Statistical analyses were carried out using the R package CRAN: stats. Student's *t*-tests were used to compare diffusive and total solute fluxes, R_{min} and TOU, and measured and expected solute flux ratios ($R_{Ca:TA}$). Grubb's test was used to identify outliers in the analysis of solute flux measurements. Correlation analysis (Pearson's *r*) was used to examine associations between variables, including correlations between the inventory of solid phase compounds and incubation time, and between solute fluxes or flux ratios and e-SOx activity according to $J_{current}$ or the incidence of the e-SOx pH signature. One-way analysis of variance (ANOVA) was used to explore the effect of incubation time on solute fluxes.

3. RESULTS

3.1. Microsensor profiling

In oxic core incubations, the distributions of porewater O_2, pH and H_2S (Fig. 2 and Table 1) revealed a build-up of the characteristic geochemical fingerprint of electrogenic sulfide oxidation, as has been observed previously in similar laboratory inductions of e-SOx (Risgaard-Petersen et al.,

2012; Malkin et al., 2014; Schauer et al., 2014; Vasquez-Cardenas et al., 2015). The development of this geochemical fingerprint is interpreted as a build-up in e-SOx activity over time associated with the establishment of a population of filamentous cable bacteria. Previous studies have shown a close link between the appearance of the e-SOx geochemical fingerprint and the downward expansion of the cable bacteria filament network (Schauer et al., 2014; Vasquez-Cardenas et al., 2015). The presence of cable bacteria filaments (*Desulfobulbaceae*, Deltaproteobacteria) in the suboxic zone of oxic cores in this study at T14 and T35 was confirmed by FISH (Fig. 3). In contrast to previous experiments, this study also captured a weakening of this geochemical fingerprint by the last time point (T71), indicating a wax and wane in e-SOx activity over time.

The O_2 penetration depth stayed nearly constant between T0 and T35, then nearly doubled at T71 (Table 1). The sulfide horizon initially matched the O_2 penetration depth (no suboxic zone was present at T0 and T7), then it increased at T14, reached its maximal value at T35, then migrated back upward by T71. The maximal thickness of the suboxic zone, reached by T35, was 1.5 cm (Fig. 2 and Table 1), which is within the range of 1.2–2.0 cm observed in other laboratory experiments (Nielsen et al., 2010; Risgaard-Petersen et al., 2012; Schauer et al., 2014) and
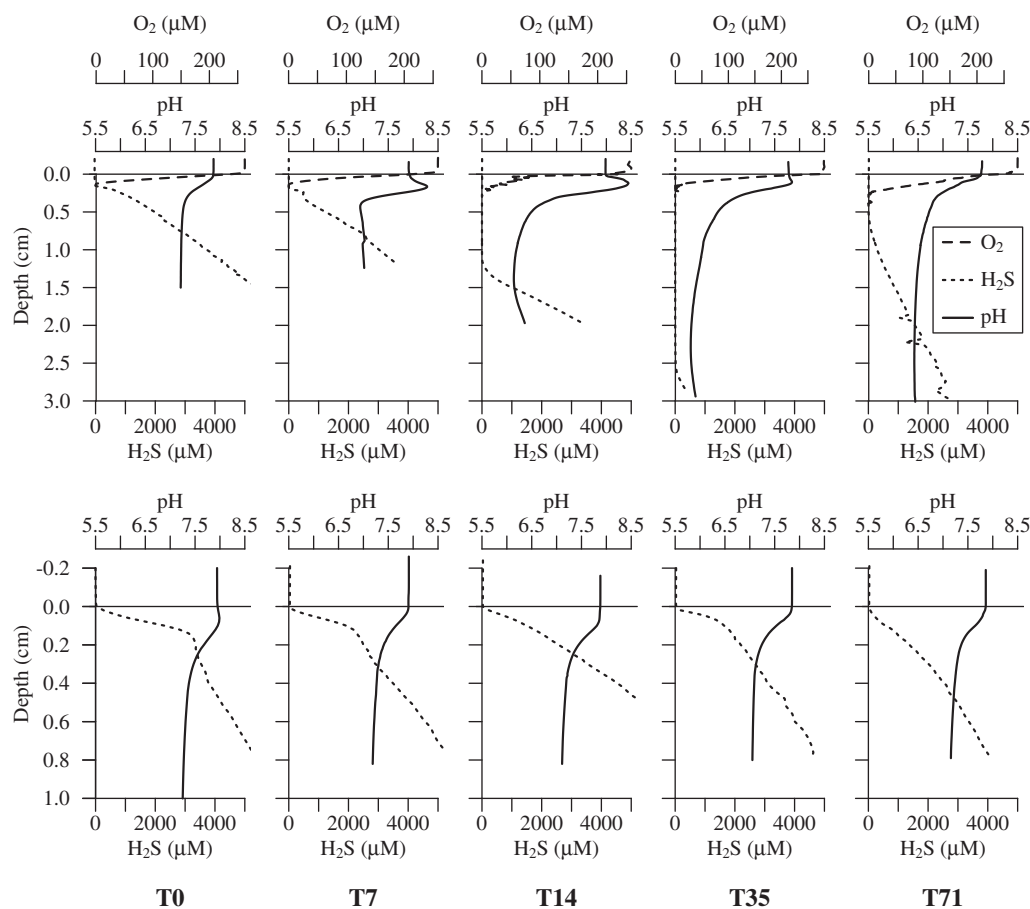

Fig. 2. Example O_2, pH and $\sum H_2S$ microprofiles in oxic (top row) and anoxic incubations (bottom row) from sampling period T0 (left) to T71 (right).

Table 1
Summary of parameters derived from porewater solute microprofiles, including O_2 penetration and H_2S horizon depths, pH maxima, minima, and the observed incidence of the e-SOx pH signature, which represents the fraction (0–1) of pH microsensor profiles measured in each core that present the characteristic signature described in Section 3.1. Values represent the mean $\pm$ 1 s.d. of all microprofiles in 3 replicate oxic or 2 replicate anoxic cores. In oxic cores, the total number of replicate profiles of each solute, n, was equal to 6 on T0, 9 on T7, 8 on T14, 10 on T35, and 9 on T71. In anoxic cores, $n = 4$ at all time points.

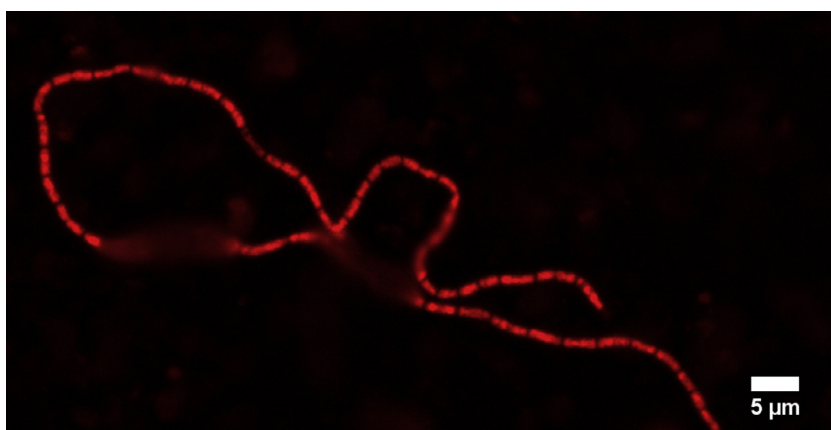|	T0	T7	T14	T35	T71
O_2 penetration depth (cm)	0.15 ± 0.02	0.16 ± 0.00	0.15 ± 0.08	0.15 ± 0.03	0.32 ± 0.04
H_2S horizon depth (cm)	0.12 ± 0.02	0.18 ± 0.08	1.13 ± 0.39	1.87 ± 0.43	1.25 ± 0.66
e-SOx pH signature					
Oxic cores					
Incidence	0 ± 0	0.33 ± 0.33	1 ± 0	0.81 ± 0.17	0.11 ± 0.19
pH maximum	7.84 ± 0.01	7.97 ± 0.06	8.32 ± 0.10	7.92 ± 0.08	7.69 ± 0.03
pH minimum	7.21 ± 0.02	6.99 ± 0.12	6.24 ± 0.11	5.94 ± 0.11	6.42 ± 0.06
Anoxic cores					
Incidence	1 ± 0	0.25 ± 0.35	0 ± 0	0 ± 0	0 ± 0
pH maximum	7.97 ± 0.01	7.92 ± 0	7.87 ± 0	7.83 ± 0.02	7.87 ± 0.02
pH minimum	7.24 ± 0.01	7.17 ± 0.02	7.10 ± 0	7.11 ± 0.07	7.18 ± 0.03

Fig. 3. Cable bacteria in incubated sediment from 2.7 to 3 cm depth in an oxic core sampled at T35, identified using FISH (DSB706 probe).

field studies (Malkin et al., 2014). The variability in O_2 penetration depth between replicate cores was small, but the variability in the sulfide horizon depth was larger, particularly toward the later stages of the experiment (Table 1). This suggests that the decline in e-SOx activity was consistent, but that replicate cores showed small differences in the timing of the e-SOx decline.

The pH distribution characteristic of e-SOx developed gradually in oxic cores (Fig. 2). Intriguingly, a distinct pH maximum was already present at T7, before the development of a suboxic zone, and increased with time, reaching 8.32 by T14 (Fig. 2 and Table 1). Beneath the subsurface maximum, pH dropped sharply and remained constant with depth. The subsurface pH maximum declined at T35 and disappeared by T71 (Table 1). Over the same period, the pH minimum broadened gradually and became more acidic from T0 to T35 (Fig. 2 and Table 1). By the end of the experiment (T71), porewater pH below the oxic layer had increased again alongside the decline in e-SOx activity. In anoxic control cores, H_2S showed a strong accumulation with depth suggesting intense sulfate reduction (Fig. 2). Porewater pH declined monotonically with depth in the

sediment, except in the first week, when small surface pH peaks were occasionally observed (Table 1). A pH maximum was present in all profiles at T0 and 25% of profiles measured at T7, but was no longer observed beyond the first week of the experiment, suggesting that these peaks were due to a transient phenomenon at the start of incubations. As H_2S always extended to the sediment–water interface in control cores, proton consumption in surface sediments may have been the result of sulfide oxidation with O_2 to elemental sulfur ($HS^- + \frac{1}{2}O_2 + H^+ \rightarrow S^0 + H_2O$) in the presence of trace amounts of O_2 present at the start of incubations. Alternately, the initial exposure to O_2 may have resulted in the production of metal oxides in the top millimeters of sediment, which may have been reduced by organic matter or sulfide when the cores were sealed, generating alkalinity (e.g., $8FeOOH + H_2S + 14H^+ \rightarrow 8Fe^{2+} + SO_4^{2-} + 12H_2O$) and producing the pH maxima observed at the start of incubations. Since porewater and solid phase analyses in anoxic cores were only conducted at the end of the experiment (T71), we cannot resolve the true origin of the initial pH peaks in anoxic cores with certainty. These transient processes may also

be partly responsible for surface pH peaks observed within the first week of oxic core incubations, prior to the establishment of a thick suboxic zone associated with e-SOx.

3.2. Oxygen uptake and current density

Diffusive O_2 uptake (DOU, Table 2) and total O_2 uptake (TOU, Table 3 and Fig. 4a) followed a similar pattern over time, increasing slightly from T0 to T7, rising sharply at T14 and declining to T71. The strong correlation between TOU/DOU and the incidence of the e-SOx pH signature (Pearson's $r_3 = 0.86/0.95$, $p < 0.05$) suggests that changes in O_2 uptake were linked to the development and decline of e-SOx in oxic cores. TOU was significantly higher at T0 relative to T71 (Student's t, 1-tailed: $t_{2.99} = 3.32$, $p = 0.02$), but this difference was not significant for DOU ($t_{2.01} = 0.87$, $p = 0.24$). Moreover, TOU was not significantly different from DOU (Student's t, 2-tailed: $-4 < t_2 < -0.5$, $p > 0.05$) except at T35 ($t_2 = -11.3$, $p < 0.01$), when mean DOU exceeded TOU by a factor of 2 (Figs. 3 and 4). Discrepancies between DOU and TOU are most likely due to spatial variability in porewater O_2 distributions and in the timing of e-SOx development and decline, as discussed in Section 3.1. While microelectrode profiles are measured at specific points in the sediment, solute flux measurements integrate over whole cores and as a result display less variability (Table 3). We therefore focus on TOU in the following sections as a more robust measure of O_2 uptake in the sediment.

Cathodic O_2 reduction represents the fraction of TOU in sediments fueling the cable bacteria metabolism. We calculated the rate of cathodic O_2 reduction in two different ways. When calculated from cathodic proton consumption using the alkalinity balance method (Section 2.4), cathodic O_2 reduction increased from 0.03 mmol m^{-2} h^{-1} at T7 to a maximum of 0.17 mmol m^{-2} h^{-1} at T14 and subsequently declined, such that it accounts for at most 12% of TOU in sediments at T35. Alternatively, when cathodic O_2 reduction is calculated from changes in TOU over the course of the experiment following Vasquez-Cardenas et al. (2015), it increased from 0.11 mmol m^{-2} h^{-1} at T7 to 0.83 mmol m^{-2} h^{-1} at T14 and subsequently declined (Table 3), suggesting that it represented up to 45% of TOU at T14. The electric current density ($J_{current}$) and electric field (E) calculated from TOU-derived estimates of cathodic O_2 reduction followed similar trends, increasing from 11.79 mA m^{-2} and 3.75 mV m^{-1} at T7 to 88.98 mA m^{-2} and 28.29 mV m^{-1} at T14 and declining thereafter (Table 3 and Fig. 4). From here onwards, the current density $J_{current}$ is used as the measure of the e-SOx activity.

3.3. Solute fluxes

Solute fluxes in oxic cores showed a distinct evolution through time that closely followed the rise and fall in e-SOx activity (Table 3 and Fig. 4). One-way ANOVA confirmed a significant effect of incubation time on the flux of O_2 (TOU, $F_4 = 21.24$, $p < 0.001$), DIC ($F_4 = 5.89$,

Table 2
Summary of calculated diffusive solute fluxes (mmol m^{-2} h^{-1}). Diffusive O_2 uptake (DOU) was derived from O_2 microsensor profiles using Fick's first law (Section 2.4, mean ± 1 s.d. of 3 replicate cores), TA flux was calculated from the sum of fluxes of the major components of alkalinity (Section 2.4, mean of 2 replicate cores), while all other estimates were derived from analyses of discrete porewater samples using PROFILE (Section 2.5, mean of 2 replicate cores). Positive values denote fluxes directed into the overlying water.

	T0	T7	T14	T35	T71
O_2 flux (-DOU)					
Oxic	-1.16 ± 0.10	-1.24 ± 0.06	-2.43 ± 0.43	-2.47 ± 0.20	-0.89 ± 0.34
Mn_d flux					
Oxic	0	0.01	0.03	0.02	0.01
Control					0
Fe_d flux					
Oxic	0	0	0.09	0.07	0
Control					0
SO_4^{2-} flux					
Oxic	-0.63	-0.22	-0.02	0.43	-0.02
Control					-0.35
TA production					
Oxic	2.65	2.23	4.08	3.61	2.09
Control					1.29
Ca^{2+} production					
Oxic	0.30	0.53	2.98	1.85	0.75
Control					0.01
PO_4^{3-} production					
Oxic	0.02	0.01	0	0	0.01
Control					0.01
NH_4^+ production					
Oxic	0.27	0.26	0.20	0.14	0.13
Control					0.27
$Si(OH)_4$ production					
Oxic	0.13	0.13	0.11	0.09	0.08
Control					0.15

Table 3
Summary of measured solute fluxes (mmol m^{-2} h^{-1}) and associated parameters derived from oxic core incubations, including the organic matter remineralization rate (R_{min}), the rate of fixed nitrogen removal in sediments (N_r), the ratio of Ca^{2+} to TA flux ($R_{Ca:TA}$), and the ratio of TA to DIC flux ($R_{TA:DIC}$). Cathodic O$_2$ reduction (COR), electric current density ($J_{current}$, mA m^{-2}), and electric field (E, mV m^{-1}) were derived from changes in TOU (see Section 2.4). R_{min} and N_r are expressed in units of mmol m^{-2} h^{-1}. Values denote the mean ± 1 s.d. of $n = 3$ replicate cores, except for values marked with an asterisk (*), for which one outlier each was excluded, as described in Section 4.7. COR, $J_{current}$, and E were excluded for time points (t) at which TOU (t) $\leqslant$ TOU ($t = 0$).

	T0	T7	T14	T35	T71
O$_2$ (-TOU)	−1.01 ± 0.09	−1.12 ± 0.05	−1.84 ± 0.20	−1.22 ± 0.22	−0.82 ± 0.05
DIC	1.24 ± 0.36	1.95 ± 0.46	2.98 ± 0.42	2.87 ± 0.70	1.28 ± 0.88
TA	0.60 ± 0.35	1.95 ± 1.10	5.67 ± 0.88	3.29 ± 1.24	1.68 ± 0.27
Ca^{2+}	0.34 ± 0.22	0.91 ± 0.46	2.00 ± 0.24	1.73 ± 0.31	0.57 ± 0.45
NH$_4^+$	0.14 ± 0.03	0.15 ± 0.01	0.06 ± 0.02	0.01 ± 0	0.01 ± 0.02
$\sum$NO$_x$	−0.05 ± 0.04	−0.02 ± 0.01	0.01 ± 0.02	0.06 ± 0.01	0.05 ± 0.01
PO$_4^{3-}$	0.10 ± 0.04	0.01 ± 0	0 ± 0	0 ± 0	0 ± 0
Si(OH)$_4$	0.09 ± 0.05	0.08 ± 0.01	0.08 ± 0.01	0.09 ± 0	0.08 ± 0.01
COR	–	0.11 ± 0.10	0.83 ± 0.22	0.21 ± 0.24	–
$J_{current}$	–	11.79 ± 10.72	88.98 ± 23.59	22.51 ± 25.73	–
E	–	3.75 ± 3.41	28.29 ± 7.50	7.16 ± 8.18	–
R_{min}	0.89 ± 0.16	1.03 ± 0.02	0.98 ± 0.35	1.14 ± 0.72	0.71 ± 0.46
N_r	0.00 ± 0.09	−0.01 ± 0.02	0.04 ± 0.03	0.05 ± 0.09	0.02 ± 0.07
$R_{Ca:TA}$	0.57 ± 0.04	0.48 ± 0.05	0.36 ± 0.03	0.43 ± 0.05*	0.45 ± 0*
$R_{TA:DIC}$	0.45 ± 0.16	0.95 ± 0.36	1.90 ± 0.10	1.13 ± 0.15	1.07 ± 0.20*

$p = 0.01$), TA ($F_4 = 15.42$, $p < 0.001$), and Ca^{2+} flux ($F_4 = 12.61$, $p < 0.001$).

In parallel with $J_{current}$, the flux of DIC, TA, and Ca^{2+} increased to maximum values at T14 and declined thereafter (Table 3 and Fig. 4). Temporal changes in fluxes, however, depended on the solute. At their peak (T14), average TA, Ca^{2+}, DIC and O$_2$ (TOU) fluxes had increased 9.5× and 5.9×, 2.4× and 1.8×, respectively, compared to initial (T0) fluxes. After T14, a decline in $J_{current}$ and fluxes of O$_2$ (TOU), DIC, TA, and Ca^{2+} was observed. At the final time point (T71), DIC and Ca^{2+} fluxes were not significantly different from T0.

Organic matter remineralization rate (R_{min}, Table 3) did not vary significantly with incubation time in oxic cores (1-way ANOVA $F_4 = 0.44$, $p = 0.78$). R_{min} was significantly lower than TOU only at T7 (Student's t, 1-tailed: $t_2 = 3.71$, $p = 0.03$) and T14 ($t_2 = 4.21$, $p = 0.03$), when $J_{current}$ and the incidence of the e-SOx pH signature were on the rise (Table 1).

The mean silicate flux did not change consistently throughout incubations (Fig. 4 and Table 3; 1-way ANOVA $F_4 = 0.21$, $p = 0.93$). However, 1-way ANOVA confirmed a significant effect of incubation time on the flux of NH$_4^+$ ($F_4 = 33.78$, $p < 0.001$), $\sum$NO$_x$ = [NO$_3^-$] + [NO$_2^-$] ($F_4 = 11.72$, $p < 0.001$), and PO$_4^{3-}$ ($F_4 = 14.5$, $p < 0.001$). Ammonium flux was highest at the start of the experiment, declined sharply after T7, and was not significantly different from 0 at T71 (Fig. 4). The flux of $\sum$NO$_x$ was directed into the sediment at T0, but gradually reversed over time, with fluxes directed out of the sediment at T35 and T71. Phosphate efflux averaged $0.10 ± 0.04$ mmol m^{-2} h^{-1} at the start of the experiment, after which it declined sharply and remained close to 0 for the duration of the experiment.

3.4. Sediment properties

Sediment porosity declined from 0.94 at the surface to 0.90 at 4 cm depth and then decreased more slowly to 0.89 at 10 cm depth.

The development of e-SOx in oxic core incubations was accompanied by the dissolution of carbonate and sulfide minerals and the precipitation of iron (oxy)hydroxides, as well as the accumulation of organic matter (Figs. 5 and 6). At the start of the experiment (T0), the total organic carbon (TOC) content of the upper 5 cm of sediment in oxic incubations averaged $3.24 ± 0.08\%$ and showed no trend with depth, as expected for homogenized sediment. Over time, a net increase in TOC content was observed in the upper 2 cm of sediment (Fig. 5). As a result, the TOC inventory in surface sediment increased significantly over time (Pearson's $r_8 = 0.63$, $p = 0.03$; Fig. 6), and the mean TOC content in the upper 5 cm of sediment at the end of the experiment (T71) reached $3.52 ± 0.14\%$. However, no change in surface sediment TOC content was apparent in anoxic incubations sampled at T71 relative to T0 (Figs. 5 and 6). The evolution of TOC content in deeper sediments is more difficult to interpret due to a greater variability between cores. The organic C:N ratio ($9.18 ± 0.18$) did not vary consistently with depth or incubation time in oxic or anoxic incubations.

The total inorganic carbon (TIC) content of the upper 5 cm of sediment averaged $2.58 ± 0.13\%$ at T0, and showed no consistent variation with depth (Fig. 5). TIC profiles in oxic cores showed net carbonate dissolution over time in the upper 3 cm of sediment (Fig. 5), resulting in a significant decline in the TIC inventory in surface sediments (Fig. 6; Pearson's $r_8 = -0.70$, $p = 0.01$) despite the variability
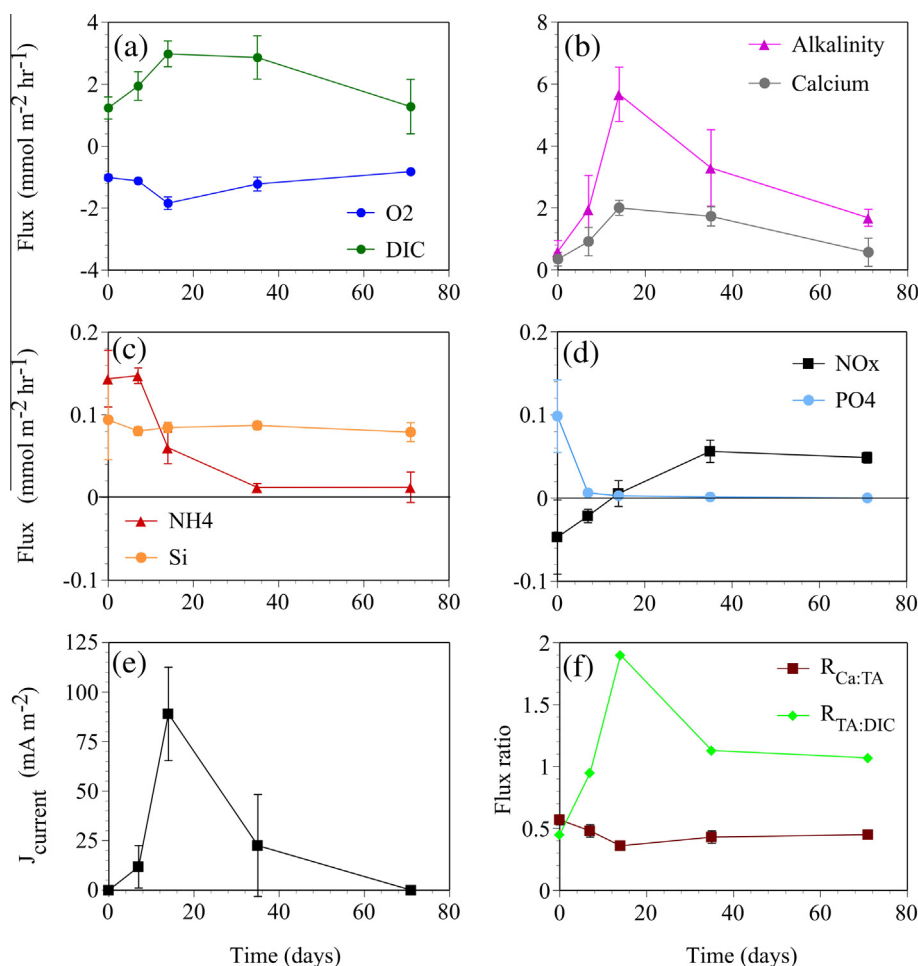
Fig. 4. Summary of the evolution of measured solute fluxes over time in oxic sediment incubations: (a) O_2 and DIC, (b) TA and Ca^{2+}, (c) NH_4^+ and $Si(OH)_4$, (d) $\sum NO_x$ and PO_4^{3-}, (e) $J_{current}$, and (f) flux ratios $R_{Ca:TA}$ and $R_{TA:DIC}$. Positive values denote fluxes directed into the overlying water.

observed between replicate cores, particularly at T71. As a result, the mean TIC content in the upper 5 cm of sediment decreased to $2.36 \pm 0.43\%$ by the end of the experiment (T71). Unlike in oxic cores, no change was observed in sediment TIC content in anoxic incubations sampled at T71 relative to T0 (Fig. 5).

As expected in homogenized sediment, the initial profiles of acid-volatile sulfur (AVS), elemental sulfur (S^0), chromium reducible sulfur (CRS), amorphous iron oxides (Fe_{ASC}) and total reactive iron (Fe_{DCA}) showed no consistent variation with depth, apart from a slight enrichment in S^0 in the upper 1 cm of sediment (Fig. 5). Initially, $56.94 \pm 5.47\%$ of the sediment sulfur content was in the form of AVS (124.72 ± 11.99 $\mu mol\ g^{-1}$, 0–10 cm depth average), $43.06 \pm 4.41\%$ in the form of CRS (94.32 ± 9.67 $\mu mol\ g^{-1}$, 0–10 cm depth-average), and $0.79 \pm 0.22\%$ in the form of S^0 (1.73 ± 0.49 $\mu mol\ g^{-1}$, 0–10 cm depth-average), assuming that S^0 is included in the CRS operational fraction. Sediment AVS content varied with time and depth. In the top 2 cm of sediment, AVS was depleted over time (Fig. 6, Pearson's $r_8 = -0.99$, $p < 0.001$). However, AVS accumulated between 2 and 3 cm depth (Fig. 6, Pearson's

$r_8 = 0.96$, $p = 0.01$), leading to a consistent enrichment in AVS profiles at this depth on T35 and T71, despite the variability observed between duplicate cores (Fig. 5). The AVS content in anoxic controls sampled at T71 averaged 129.69 ± 20.47 $\mu mol\ g^{-1}$ from 0 to 10 cm, and did not show any consistent variation with depth or incubation time.

Sediment S^0 and CRS content similarly varied with depth and incubation time. In the upper 2 cm of sediment, CRS and S^0 were depleted over time (Fig. 6, CRS: Pearson's $r_8 = -0.95$, $p < 0.001$; S^0: Pearson's $r_8 = -0.94$, $p < 0.001$). In deeper sediment, CRS and S^0 inventories did not vary consistently with time, but CRS profiles showed a subsurface enrichment, resulting in a CRS peak around 3 cm depth at T71, similar to but smaller than that observed in AVS (Fig. 5). CRS and S^0 content in anoxic cores at T71 averaged 86.19 ± 19.74 $\mu mol\ g^{-1}$ and 1.88 ± 0.36 $\mu mol\ g^{-1}$ from 0 to 10 cm, and did not show consistent variations with depth or incubation time.

Depth-averaged total reactive iron in oxic cores ($Fe_{DCA} = 235.95 \pm 7.19$ $\mu mol\ g^{-1}$, 0–10 cm, T0-T71) remained relatively constant over time, with the exception of one core at T35 that displayed an anomalously high
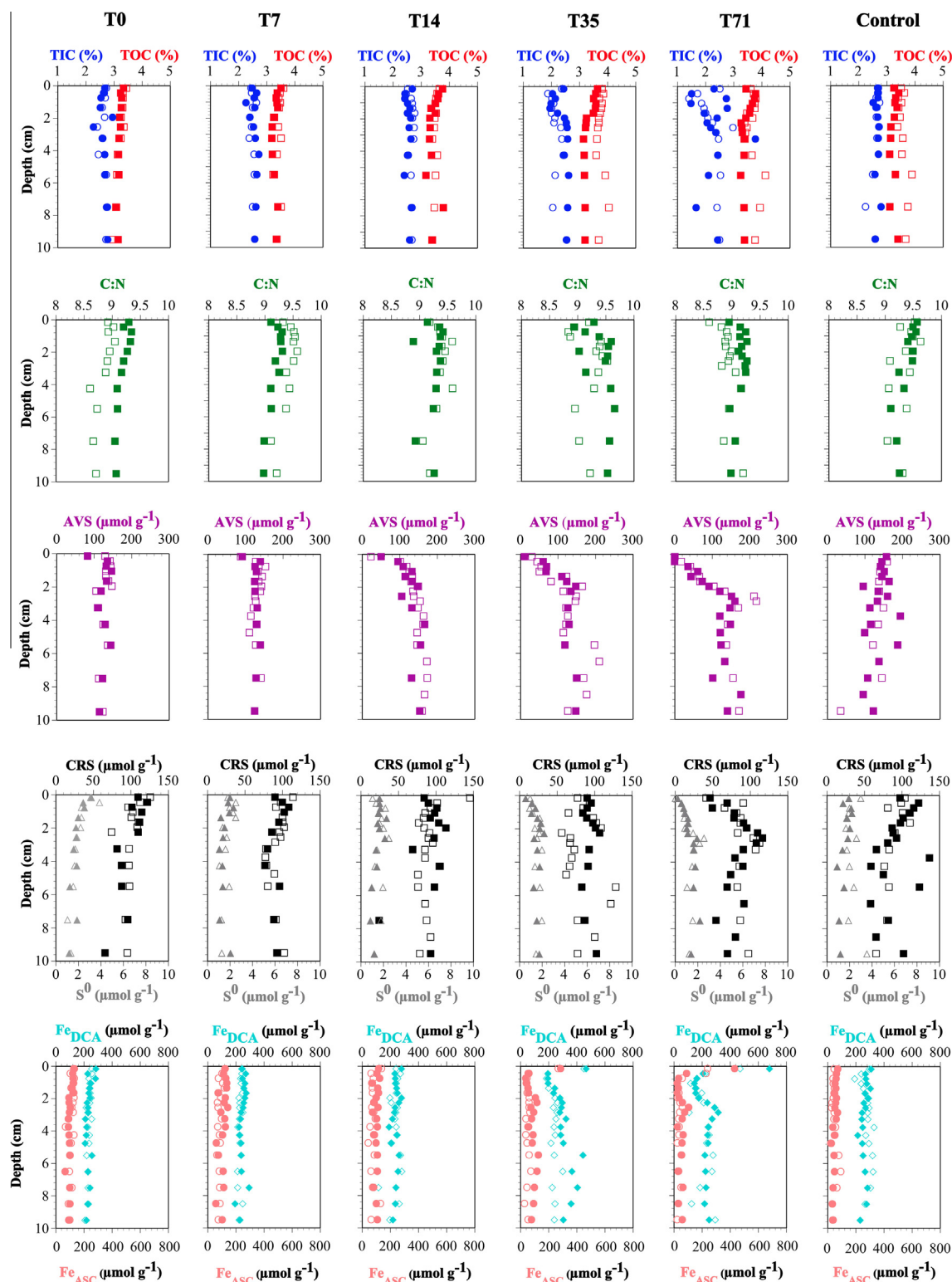
Fig. 5. The evolution of sediment geochemistry over time (T0–T71) in oxic incubations and anoxic controls (right), including duplicate profiles of sediment organic carbon, inorganic carbon, organic C:N ratio, acid volatile sulfide (AVS), chromium reducible sulfide (CRS), elemental sulfur (S^0), and reactive iron in dithionite extractions (Fe_{DCA}) and ascorbate extractions (Fe_{ASC}). Concentrations are expressed either in μmol (g dry sediment)$^{-1}$ or % (100 × g per g dry sediment).
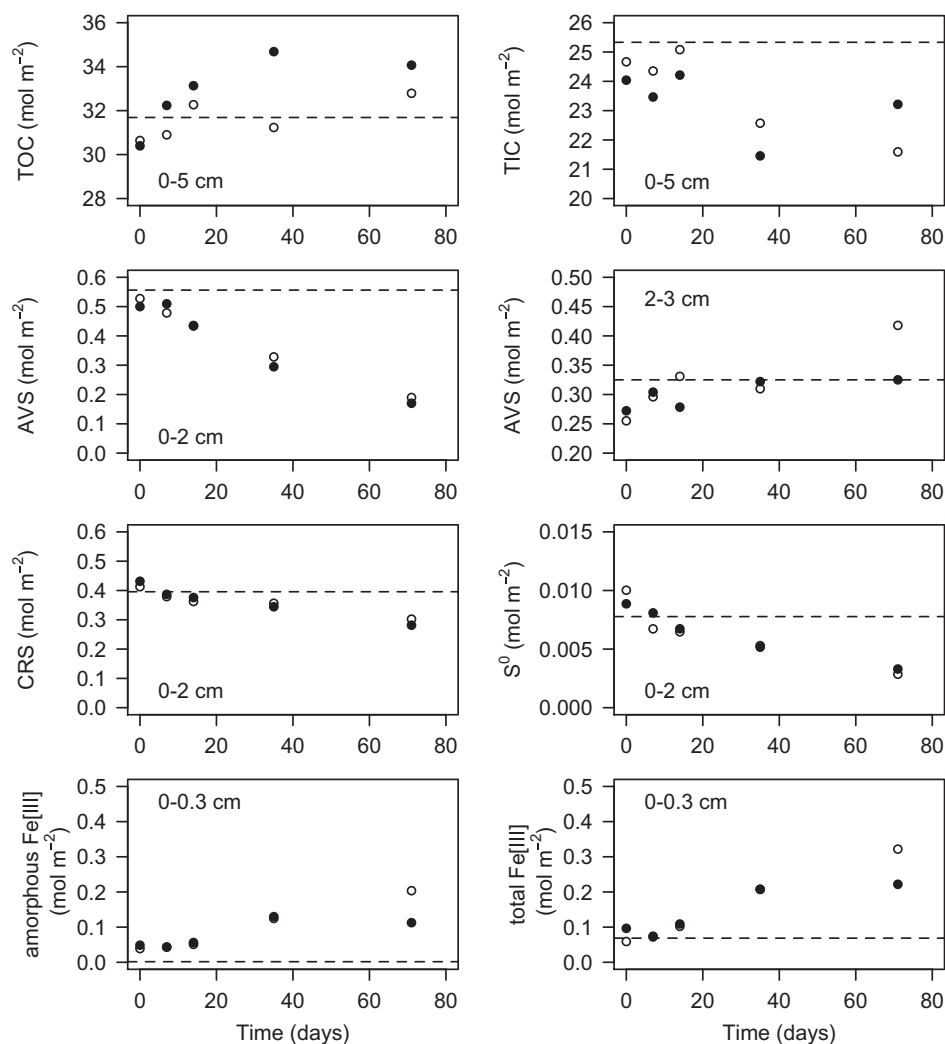
Fig. 6. The temporal evolution of sediment inventories of organic and inorganic carbon, AVS, CRS, S⁰, FeASC and FeDCA in oxic cores, integrated over defined depth intervals. Duplicate oxic cores are shown in open and filled circles. Dashed lines represent sediment inventories integrated over equivalent depth intervals in anoxic cores sampled at T71.

Fe_{DCA} content (330.32 µmol g^{-1}). Dithionite extracts AVS nearly quantitatively (Canfield et al., 1993), but only about 35% of AVS was leached by ascorbate, based on a comparison of AVS and Fe_{ASC} in control cores. Despite the large variability in solid phase analyses, a comparison of Fe_{DCA}, Fe_{ASC} and AVS at 2–3 cm depth at T71 indicates that Fe_{DCA} and Fe_{ASC} peaks likely reflect the buildup in AVS at this depth. Average Fe_{ASC} content at 2–3 cm depth in duplicate cores (64 µmol/g) is comparable to the ascorbate leachable fraction (35%) of average AVS content (58 µmol/g) at this depth at T71; and the average Fe_{DCA} buildup at 2–3 cm depth relative to the 5–10 cm depth horizon (28 µmol g^{-1}) matches AVS accumulation at this depth (23 µmol g^{-1}). We define amorphous Fe[III] as Fe_{ASC} minus the portion of AVS leached by ascorbate, and total Fe[III] as Fe_{DCA} minus all Fe in AVS, following Kostka and Luther (1994). Both amorphous and total Fe[III] increased with time in the surface 0.3 cm of sediments (Fig. 6, Pearson's $r_8 = 0.88$ and 0.93, $p < 0.001$), and

amorphous phases account for a large part of the Fe that precipitated in surface sediments. In anoxic controls, the depth-averaged total reactive Fe content at T71 (Fe_{DCA} 271.86 ± 21.90 µmol g^{-1}) was greater than in oxic cores, but no consistent vertical trends were observed (Fig. 5).

3.5. Porewater solute distributions

Porewater geochemistry responded strongly to the development and decline of e-SOx. The rise in e-SOx activity in oxic cores was accompanied by the development of a subsurface maximum in dissolved Fe (Fe_d), which reached 612 µmol L^{-1} at T35 and was attenuated by T71 (Fig. 7). Over time, the Fe_d maximum broadened and its peak tracked the bottom of the suboxic zone as it moved deeper, from ~0.3 cm depth at T7 to ~2 cm at T35 and T71. This distribution reflects the mobilization of Fe_d in the suboxic zone and removal above and below. Both mobilization and removal moved deeper with time, with rates increasing
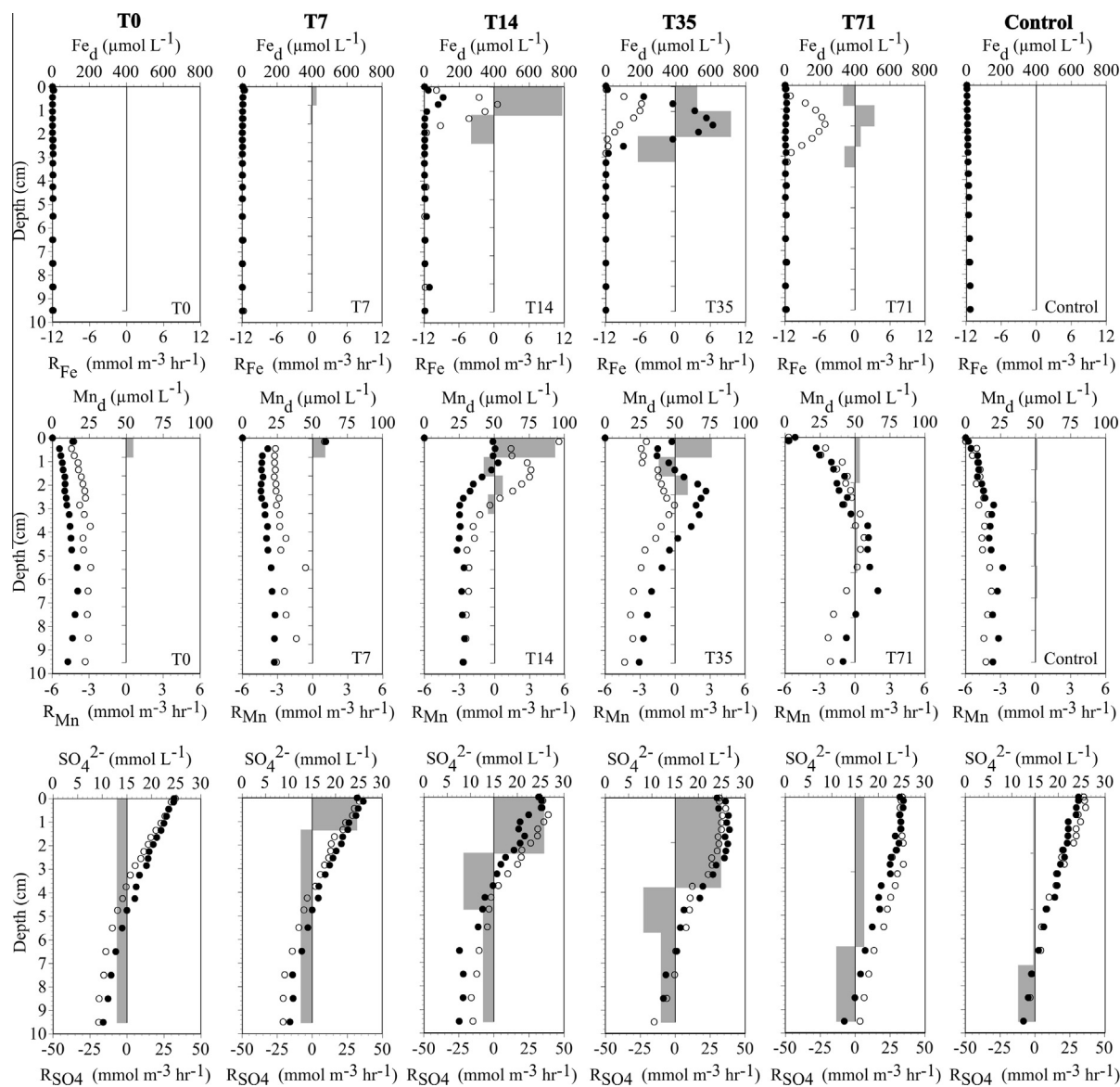
Fig. 7. The evolution of porewater Fe_d (top row), Mn_d (middle row), and SO_4^{2-} (bottom row) concentration profiles in oxic cores over time (from left to right, T0 to T71) and in anoxic controls (far right). Gray bars represent production/consumption rates (R) of each solute estimated from the average of duplicate profiles of porewater solute concentrations using PROFILE (see Section 2.5).

to T14 or T35 and attenuating thereafter. The upward diffusive flux of Fe_d also peaked at T14 and declined thereafter (Table 2). Anoxic cores displayed no subsurface maximum at T71, and only a slight accumulation of Fe_d was observed, as concentrations remained below 12 μmol L^{-1} (Fig. 7).

Dissolved Mn (Mn_d) profiles in oxic cores developed double maxima in parallel with the rise in e-SOx activity. A surface peak in the upper 0.3 cm of sediment reached 96 μmol L^{-1} at T14, while a broader and deeper secondary peak reached 76 μmol L^{-1} at ∼2 cm depth (Fig. 7). Both peaks were subsequently attenuated over time, while the second peak broadened and deepened with time. These peaks reflect two zones of net Mn_d mobilization separated by a layer of net removal. Mn_d mobilization rates in sediments (Fig. 7) and its upward diffusive flux (Table 2)

peaked at T14 and declined thereafter. At the final time point (T71), porewater Mn_d in oxic cores remained higher than in anoxic controls (Fig. 7). Mn_d profiles in anoxic controls at T71 were similar to initial profiles (T0), and remained below 26 μmol L^{-1} (Fig. 7). Differences in the depth and magnitude of Mn_d and Fe_d peaks are evident between duplicate cores, and are most likely due to variability in the timing of e-SOx development and decline between cores.

In oxic cores at T0, porewater SO_4^{2-} declined monotonically with depth from about 25 mM in the overlying water to about 9 mM at 10 cm depth in the sediment (Fig. 7). A two-layer SO_4^{2-} profile developed by T14 concurrent with the rise in e-SOx. In the upper 2–3 cm of sediment, there was little or no change in porewater SO_4^{2-}, and profile

analysis revealed a production of SO_4^{2-}. This zone of SO_4^{2-} production persisted through the end of the experiment, and the transition zone gradually deepened from ∼1 cm at T7 to ∼6 cm at T71. The rate of SO_4^{2-} production in oxic surface sediments peaked between T14 and T35 (Fig. 7). Below this zone of SO_4^{2-} production, there was a zone of SO_4^{2-} removal, indicative of sulfate reduction. Diffusive flux calculations based on SO_4^{2-} profiles revealed a reversal, from a strong SO_4^{2-} influx at T0 to a strong efflux by T35, weakening by T71 (Table 2). Porewater SO_4^{2-} in anoxic cores declined monotonically with depth (Fig. 7), indicative of sulfate reduction throughout the entire depth range (0–10 cm). Diffusive SO_4^{2-} influx was lower and porewater SO_4^{2-} at 10 cm depth (between 12 and 13 mM) was higher at T71 than at T0, reflecting lower SO_4^{2-} reduction rates than at T0.

Porewater TA generally increased from 2.4–2.6 mM in the overlying water to 21–28 mM at 10 cm depth in the sediment (Fig. 8). A distinct TA distribution developed in oxic cores by T14, in concert with e-SOx development. A sharp increase in porewater TA appeared at the sediment–water interface, and further analysis of TA profiles revealed the production of TA in surface sediments. This feature persisted through the end of the experiment, and TA production rates peaked between T14 and T35. TA increased more slowly with depth in the suboxic zone, and profile analysis revealed the development of a zone of TA

consumption at 1–2 cm depth in the sediment, which peaked at T35 (Fig. 8). Below 2 cm, TA concentrations increased more sharply with depth. Diffusive TA efflux at the sediment–water interface peaked at T14, and declined subsequently thereafter (Table 2). Diffusive TA flux estimates were not significantly different from direct measurements of net TA efflux (Tables 2 and 3), except at T0 (Student's t, 2-tailed: $t_2 = -10.14$, $p = 0.01$). In anoxic cores, porewater TA increased monotonically with depth at T71 (Fig. 8). Calculated diffusive TA efflux and porewater TA concentrations at 10 cm depth (between 21 and 22 mEq L^{-1}) were lower in anoxic controls at T71 than at T0, reflecting lower net production in sediments than at T0 (Fig. 8 and Table 2).

Porewater Ca^{2+} varied between 9 and 10 mM at T0, and a small maximum appeared in the upper 1 cm of sediment in one of two replicate cores (Fig. 8). In parallel with the rise in e-SOx activity in oxic cores, the surface Ca^{2+} peak became deeper, broader, and more intense over the course of the experiment. Maximum Ca^{2+} concentrations peaked between T14 and T35, reaching 22 mM at 2.3 cm depth on T35, and declined thereafter (Fig. 8). The rate of Ca^{2+} release in sediments and the resulting diffusive efflux of Ca^{2+} at the sediment–water interface peaked at T14 (Fig. 8 and Table 2). Diffusive Ca^{2+} flux estimates were not significantly different from direct measurements of net Ca^{2+} efflux (Fig. 4; Student's t, 2-tailed: $t_4 = -0.77$,
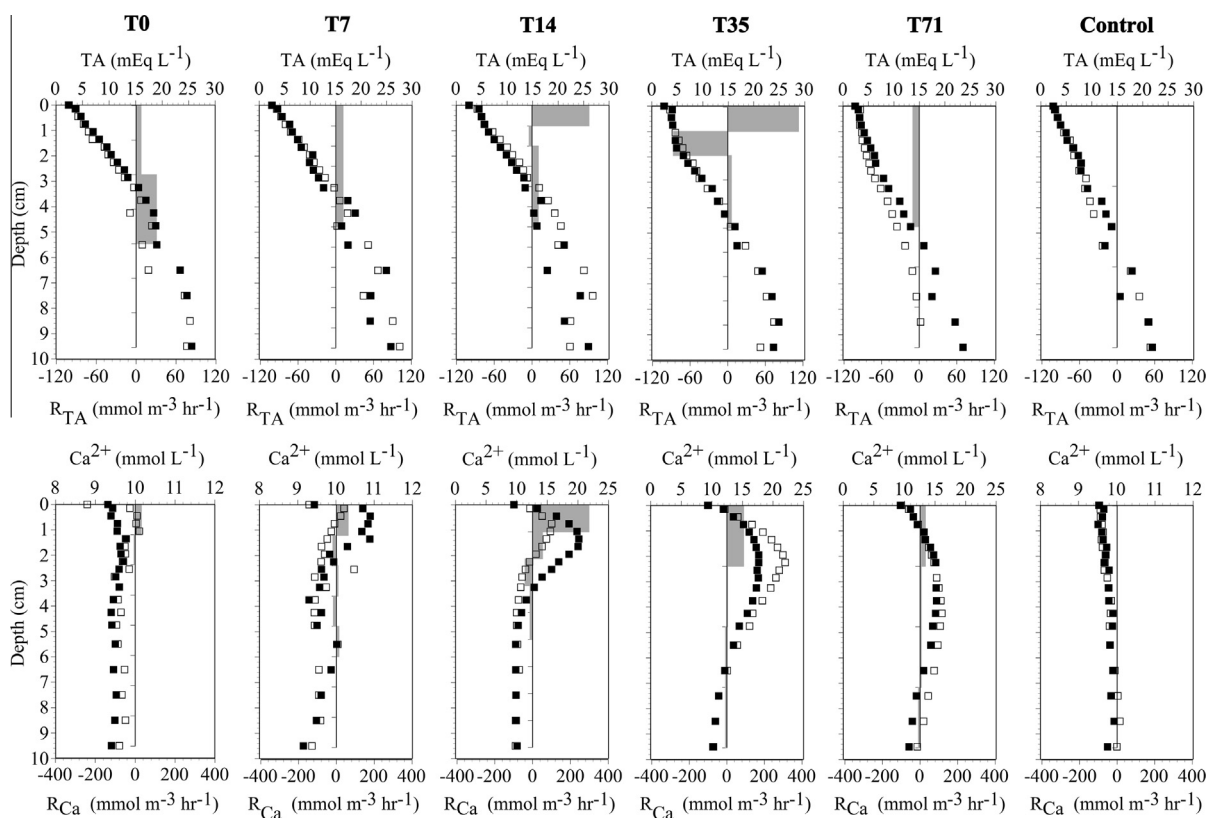

Fig. 8. The evolution of porewater TA (top row) and Ca^{2+} (bottom row) profiles in oxic cores over time (T0 to T71 from left to right) and in anoxic controls (far right). Gray bars represent production/consumption rates (R) of each solute estimated from the average of duplicate profiles of porewater solute concentrations using PROFILE (see Section 2.5).

$p = 0.48$). In anoxic cores sampled at T71, porewater Ca^{2+} increased monotonically with depth and remained below 10 mM (Fig. 8). Diffusive Ca^{2+} flux at the sediment–water interface was lower in anoxic cores at T71 than in oxic cores at T0 (Table 2).

Dissolved inorganic nutrient (PO_4^{3-}, NH_4^+, $Si(OH)_4$) concentrations increased with depth in the sediment, due to remineralization (Fig. 9). Remineralization rates and calculated diffusive fluxes of $Si(OH)_4$ and NH_4^+ at the sediment–water interface decreased with time in oxic cores but not in anoxic cores (Table 2 and Fig. 9). The diffusive fluxes of $Si(OH)_4$ and NH_4^+ in anoxic cores sampled at T71 were very similar to calculated fluxes at T0. Phosphate profiles in oxic cores showed a conspicuous response to the development of e-SOx. At the start of the experiment,

porewater PO_4^{3-} gradually increased with depth, reflecting the release of PO_4^{3-} by remineralization (Fig. 9). By T14, PO_4^{3-} profiles developed a surface layer in which porewater PO_4^{3-} remained constant or increased very slowly with depth, and profile analysis revealed a reversal from PO_4^{3-} production to removal in the upper 1 cm of sediments (Fig. 9). This zone of PO_4^{3-} removal deepened to 2 cm by T35, and was subsequently attenuated by T71. Below this zone, PO_4^{3-} concentrations increased more strongly with depth. These changes in porewater P dynamics resulted in capping diffusive PO_4^{3-} efflux, which dropped from 0.2 mmol m^{-2} h^{-1} at T0 to 0 at T14 (Table 2). In anoxic cores sampled at T71, porewater PO_4^{3-} concentrations and diffusive fluxes resembled those observed at T0 (Fig. 9 and Table 2).
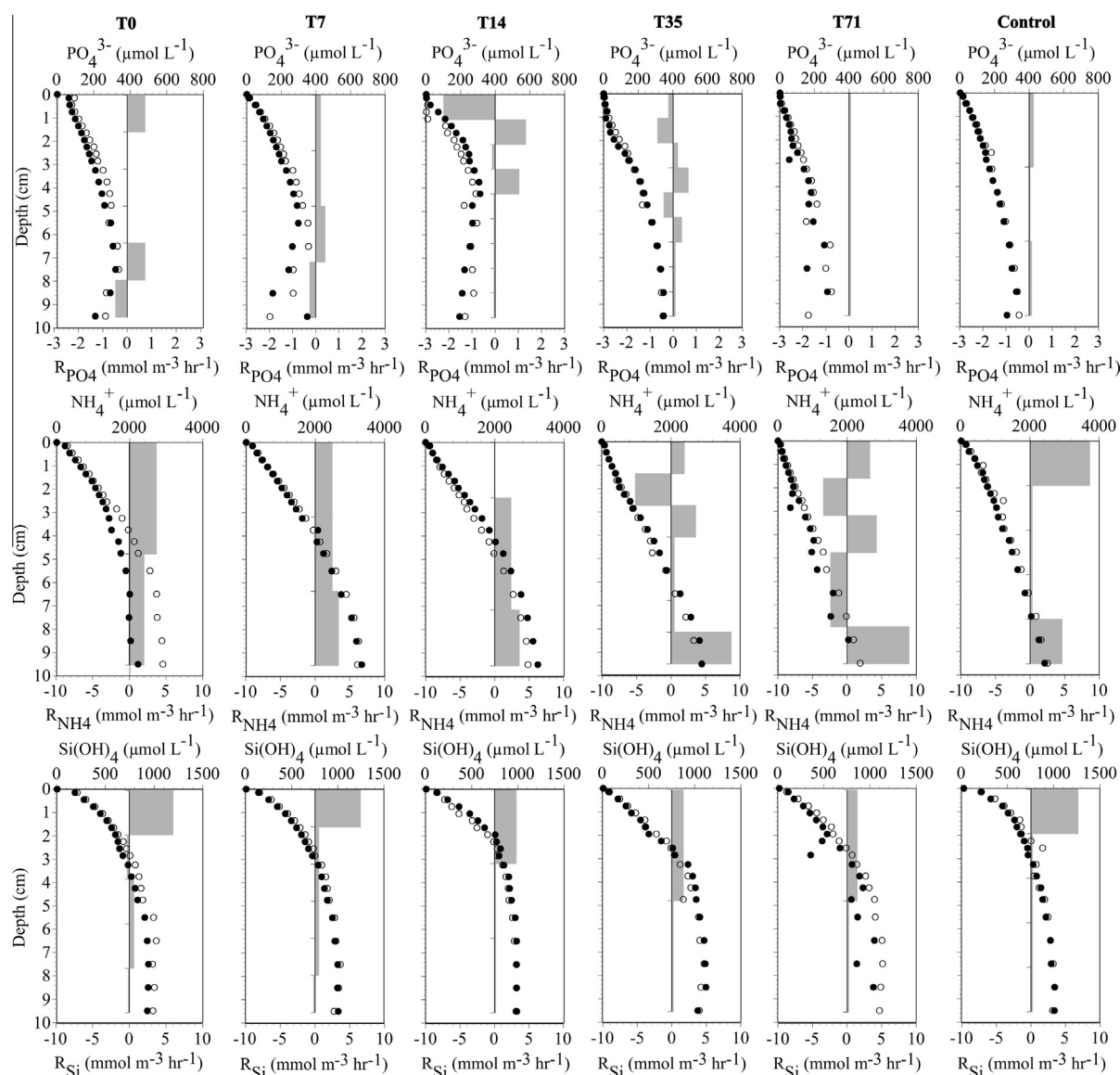

Fig. 9. The evolution of porewater PO_4^{3-} (top row), NH_4^+ (middle row), and $Si(OH)_4$ (bottom row) concentration profiles in oxic cores over time (from left to right, T0 to T71) and in anoxic controls (far right). Gray bars represent production/consumption rates (R) of each solute estimated from the average of duplicate profiles of porewater solute concentrations using PROFILE (see Section 2.5).

4. DISCUSSION

4.1. The development of e-SOx in sediments

The induction of electrogenic sulfide oxidation (e-SOx) in oxic cores is consistent with its detection in intact cores collected at the same site during a previous study (Malkin et al., 2014), and the downward growth of a cable bacteria population in a previous induction experiment with sediment from the same field site (Vasquez-Cardenas et al., 2015). Calculated rates of cathodic O_2 reduction in this study peaked after 2 weeks (0.83 mmol m^{-2} h^{-1} at T14), providing an associated current density of 89 $\pm$ 24 mA m^{-2}. This value of $J_{current}$ is lower than that obtained in a previous induction experiment with sediment from the same field site (232 mA m^{-2}; Vasquez-Cardenas et al., 2015), but considerably higher than the $J_{current}$ measured in intact cores at the same site (16–27 mA m^{-2}; Malkin et al., 2014), and similar to the value obtained in an induction experiment using sediment from the Baltic sea (95 mA m^{-2}; Schauer et al., 2014).

A marked temporal evolution was observed in the rate of e-SOx in this study. Consistent changes in the incidence and intensity of pH extremes, the vertical separation of O_2 penetration and H_2S horizon depths (Fig. 2 and Table 1), calculated $J_{current}$, cathodic O_2 reduction, and O_2 uptake (DOU and TOU, Tables 2 and 3) show the build-up of e-SOx activity, reaching a maximum at T14, and subsequently declining to the end of the experiment (T71), when e-SOx was no longer apparent. The same temporal evolution in the rate of e-SOx, cable bacteria filament abundance, activity and vertical extent has been observed previously in other e-SOx induction studies (Schauer et al., 2014; Vasquez-Cardenas et al., 2015).

The remarkable observation that e-SOx vanishes after a period of weeks to months suggests that the cable bacteria population somehow collapses. One hypothesis is that this population decline results from the exhaustion of the sedimentary FeS pool (Schauer et al., 2014). Because FeS dissolution supplies a substantial part of the sulfide for e-SOx, the depletion of FeS may limit the electron donor supply for cable bacteria (Risgaard-Petersen et al., 2012). The strong depletion of FeS observed here in the top 2 cm of oxic sediment incubations (Figs. 5 and 6) is synchronous with the decline in e-SOx activity, and hence supports this hypothesis.

4.2. Electrical effects on porewater profiles and solute fluxes

When an electron current is induced in sediments, a corresponding electric field drives an ion counter-current in the porewater to maintain charge balance. Fine-scale profiles of electric potential in sediments have revealed this predicted electric field when the geochemical fingerprint of e-SOx is present (Risgaard-Petersen et al., 2014). In this study, maximum current density ($J_{current} = 89 \pm 23$ mA m^{-2}) was reached after 2 weeks (T14), producing an associated electric field (E) of 28.3 $\pm$ 7.5 mV m^{-1} (Table 3), similar in magnitude to that observed by Risgaard-Petersen et al.

(2014) in incubations of sediment sampled at Aarhus Harbor, Denmark.

The presence of an electric field may have large ramifications for the interpretation of porewater profiles and the associated fluxes of solutes, given by the Nernst–Planck equation (Risgaard-Petersen et al., 2012):

$$J = -\phi D_s \left(\frac{\partial C}{\partial x} - z \frac{FE}{RT} C \right) \qquad (2)$$

which includes a molecular diffusion component as well as a second ionic drift term caused by the electric field. In this expression, C is solute concentration, R the universal gas constant and T the absolute temperature. The quantity z denotes the ion charge, which is positive for cations and negative for anions. Accordingly, the electric field moves cations like Ca^{2+}, Fe^{2+}, Mn^{2+}, and NH_4^+ toward the sediment–water interface, with a positive (i.e. upward) flux component due to ionic drift. Conversely, for SO_4^{2-} and other anions, there is a negative (i.e. downward) flux component due to ionic drift, which moves anions into deeper sediment horizons.

When examining the effect of ionic drift on porewater profiles, one should note that (1) the electric field is only present when cable bacteria actively induce currents, i.e., in the top few centimeters of sediment, and (2) the ionic drift term scales with concentration (Eq. (2)), so the drift effect will be largest for multivalent ions with high concentrations near the sediment–water interface. As a result, in the present study, the ionic drift is most visible in Ca^{2+} and SO_4^{2-} profiles (Figs. 7 and 8). As further detailed below, Ca^{2+} and SO_4^{2-} production are in fact closely connected. Both solutes are produced in the suboxic zone, where anodic sulfide oxidation produces SO_4^{2-} (Fig. 7), acidifies the porewater (Fig. 2), and thereby drives the dissolution of FeS and carbonates (Fig. 5), producing Ca^{2+} (Fig. 8). However the build-up of Ca^{2+} and SO_4^{2-} in the porewater are very different. The subsurface SO_4^{2-} peak is flattened (Fig. 7) and production estimated using PROFILE extends down to 3.8 cm. In contrast, the subsurface build-up in Ca^{2+} is much sharper (Fig. 8), and the estimated production is limited to the first 2.4 cm. The apparent difference in the vertical distribution of estimated production rates for these two solutes is most likely not real, but an artifact of the application of PROFILE, which cannot account for ionic drift. Ca^{2+} is pushed upward by the electric field, so it appears to be produced closer to the sediment–water interface, while in reality, production occurs deeper in the suboxic zone. Using the electric field calculated above ($E = 28.3$ mV m^{-1}) and a mean Ca^{2+} concentration of 18 mM in the suboxic zone, the upward ionic drift component becomes 0.09 mmol m^{-2} h^{-1}, which represents about 5% of the overall Ca^{2+} flux out of the sediment (Table 3). Conversely, SO_4^{2-} is pulled downward into the sediment by the electric field, so it appears that it is produced deeper in the sediment, while in reality production occurs higher up in the suboxic zone. Adopting a mean SO_4^{2-} concentration of 25 mM in the suboxic zone, the ionic drift contribution for SO_4^{2-} becomes −0.17 mmol m^{-2} h^{-1}, while PROFILE predicts a diffusive SO_4^{2-} flux of

-0.02 mmol m^{-2} h^{-1} into the sediment (Table 2; T14). Accordingly, the actual SO$_4^{2-}$ flux amounts to -0.19 mmol m^{-2} h^{-1}. This analysis reveals that flux estimates for major ions in the presence of an electric field should be examined for the effect of ionic drift on porewater profiles.

4.3. Sediment community metabolism

Organic matter remineralization rates were similar in oxic and anoxic cores, and remained constant for the duration of the experiment. In oxic cores, R_{min} derived from measured DIC and Ca^{2+} fluxes did not vary over time (Table 3). In anoxic cores, R_{min} can be calculated as $2 \times J_{SO_4}$, where J_{SO_4} is the diffusive sulfate flux derived from porewater SO$_4^{2-}$ distributions using PROFILE (Table 2), assuming a 2:1 ratio for C:S in SO$_4^{2-}$ reduction. This estimate yields a mean R_{min} of 0.7 mmol m^{-2} h^{-1} in anoxic cores at T71, which is very close to the mean value of R_{min} in oxic cores in the same period (Table 3).

It has been shown that e-SOx may account for a substantial part (50–90%) of the total O$_2$ uptake in coastal sediments (Nielsen et al., 2010; Schauer et al., 2014; Vasquez-Cardenas et al., 2015). In this study, O$_2$ consumption rates (Table 3 and Fig. 4) were in the range of diffusive O$_2$ uptake rates previously measured in intact sediments at this site (Malkin et al., 2014), and in other fine-grained coastal sediments (Seitzinger et al., 1984; Gribsholt and Kristensen, 2003; Giblin et al., 2010). Total O$_2$ uptake matched R_{min} at the start (T0) and end (T71) of the experiment (Table 3), when O$_2$ consumption was predominantly associated with organic matter remineralization. Cathodic O$_2$ reduction fueled an increase in TOU relative to R_{min}, which was responsible for up to 45% of TOU at peak e-SOx activity (T14). This is in the lower range of the estimated contribution of cathodic O$_2$ reduction to TOU previously observed in laboratory e-SOx inductions with homogenized sediments (50–90%, Nielsen et al., 2010; Schauer et al., 2014; Vasquez-Cardenas et al., 2015), but greater than measurements made in intact sediments from the same site (14–34%; Malkin et al., 2014). The weaker TOU and deeper O$_2$ penetration observed at T71 relative to T0 are likely the result of the removal of $\sum$H$_2$S (Fig. 2) and FeS (Fig. 5) from surface sediments by e-SOx, as discussed in Section 4.4.

Cathodic O$_2$ reduction consumed 258 mmol O$_2$ m^{-2} during the period in which e-SOx was most active, assuming an average rate from T7 to T35. Since cathodic O$_2$ reduction consumes 4 electrons per O$_2$ molecule reduced and anodic sulfide oxidation produces 8 electrons per H$_2$S molecule oxidized, the mean rate of H$_2$S oxidation during this period must be 129 mmol m^{-2}. No measurements of sulfate reduction were undertaken in this study, so it is not possible to quantify this source of H$_2$S. Nevertheless, it is noteworthy that the expected rate of anodic sulfide oxidation is very close to the rate of AVS depletion in the upper 2 cm of sediment (Fig. 6, 0.20 mmol m^{-2} h^{-1}), which amounts to 135 mmol m^{-2} in 28 days. Although rates of Fe$_d$ production estimated with PROFILE indicate slightly lower FeS dissolution rates (0.14 mmol m^{-2} h^{-1} at T14),

the close match between the rate of electron release from the anodic oxidation of H$_2$S mobilized by FeS dissolution and the rate of electron consumption by cathodic O$_2$ reduction corroborates the earlier suggestion that FeS dissolution is the main source of H$_2$S for anodic sulfide oxidation (Risgaard-Petersen et al., 2012). These mass balance considerations provide further confirmation of cathodic O$_2$ reduction estimates derived from changes in TOU (Table 3).

4.4. Fe and S cycling

The development of e-SOx in this study coincided with the production of dissolved Fe at 1–2 cm depth (Fig. 7 and Table 1). Risgaard-Petersen et al. (2012) showed that the subsurface production of acidity by e-SOx results in FeS dissolution, which is consistent with the vertical overlap between the measured Fe$_d$ production (Fig. 7) and the pH minimum (Fig. 2) observed in this study. Here, the production of Fe$_d$ by FeS dissolution is further confirmed by the rate of Fe$_d$ production at peak e-SOx activity (T14; 0.14 mmol m^{-2} h^{-1}), calculated using PROFILE (Fig. 7), which is very near the average rate of AVS depletion measured in the top 2 cm of sediment in oxic cores (0.20 mmol m^{-2} h^{-1}; Fig. 6). Fe$_d$ mobilized by FeS dissolution at the pH minimum and diffusing downward was reprecipitated at the H$_2$S horizon (Figs. 2 and 7), as shown by the accumulation of AVS (Figs. 5 and 6) and the removal of Fe$_d$ just below the developing Fe$_d$ maximum (Fig. 7). Indeed, the Fe$_d$ removal rate at the sulfide horizon at peak e-SOx activity (T14; 0.05 mmol m^{-2} h^{-1}), calculated using PROFILE (Fig. 7), closely matches the average rate of AVS buildup measured at 2–3 cm depth in the sediment (0.05 mmol m^{-2} h^{-1}; Fig. 6). Fe$_d$ diffusing upward was reoxidized at the sediment–water interface, producing an Fe oxide crust in oxic surface sediments (Fig. 5), as previously observed by Risgaard-Petersen et al. (2012). The upward flux of Fe$_d$ at T14 (0.09 mmol m^{-2} h^{-1}; Table 2) is similar in magnitude to the average accumulation rate of amorphous Fe[III] in the upper 0.3 cm of sediment (0.07 mmol m^{-2} h^{-1}), indicating that this crust is most likely composed of an amorphous Fe oxide phase (Figs. 5 and 6).

The development of e-SOx in this experiment was accompanied by SO$_4^{2-}$ production in the suboxic zone (Fig. 7), confirming the earlier suggestion that anodic sulfide oxidation proceeds all the way to SO$_4^{2-}$ (Risgaard-Petersen et al., 2012). The rate of SO$_4^{2-}$ production by anodic sulfide oxidation at peak e-SOx activity can be estimated as the difference between the SO$_4^{2-}$ flux at the sediment–water interface in control cores and in oxic cores at T14, taking into account ionic drift (Section 4.2). This yields a SO$_4^{2-}$ production rate of 0.16 mmol m^{-2} h^{-1} at T14, which is very near the rates of Fe$_d$ production (0.14 mmol m^{-2} h^{-1}) and AVS depletion (0.20 mmol m^{-2} h^{-1}; Fig. 6) discussed above. This mass balance analysis quantitatively corroborates our current understanding of e-SOx in which H$_2$S, mainly derived from FeS dissolution, is completely oxidized to SO$_4^{2-}$ (Risgaard-Petersen et al., 2012). This mechanism of H$_2$S oxidation generates more acidity, and therefore provides stronger reinforcement of

H_2S production from FeS dissolution, a positive feedback process or metabolic "turbo" boost that fuels e-SOx (Risgaard-Petersen et al., 2012; Meysman et al., 2015).

By dissolving previously accumulated FeS and relying on the oxidation of remobilized H_2S, e-SOx forces FeS accumulation in sediments out of steady state. Therefore, the development and decline of e-SOx may cause a cyclical, perhaps seasonal, pattern of FeS depletion and accumulation in coastal sediments. Future work should address whether these patterns are observed in nature.

4.5. Mn cycling

Electrogenic sulfide oxidation resulted in strong remobilization of Mn in oxic cores. Dissolved Mn was released at 1–3 cm depth by T14 (Fig. 7), likely due to the release of Mn_d adsorbed on $CaCO_3$ or FeS surfaces (Martin and Knauer, 1984; Arakaki and Morse, 1993), as these minerals dissolve in the suboxic zone due to the production of acidity by anodic sulfide oxidation. Below about 3 cm, Mn_d diffused deeper in sediments than Fe_d (Fig. 8). Downward diffusing Fe_d was rapidly bound as FeS (Figs. 5 and 7), but the higher solubility of MnS renders its precipitation less favorable, and porewater Mn_d was most likely controlled by adsorption or co-precipitation onto calcite surfaces (Franklin and Morse, 1983). Alkalinity release by sulfate reduction favors carbonate precipitation and porewater Mn^{2+} concentrations may exceed saturation with respect to an authigenic $Ca(Mn)CO_3$ phase (Middelburg et al., 1987; Mucci, 2004). Nevertheless, inhibitors such as PO_4^{3-} and dissolved organic C hinder the nucleation and growth of carbonate minerals in coastal sediments. The lack of pH measurements below 3 cm in this experiment unfortunately precludes the determination of porewater saturation state at depth.

A closer look at Mn_d profiles reveals a surface peak indicative of Mn_d release in oxic surface sediments at T7, increasing at T14, and declining subsequently thereafter (Fig. 7). Mn_d release in surface sediments may reflect the production of soluble Mn^{3+} as Mn^{2+} diffusing upward into the oxic zone is reoxidized (Madison et al., 2013). Future studies are needed to examine the speciation of Mn release associated with e-SOx.

A most intriguing aspect of this study was the indication that e-SOx development stimulated diffusive Mn efflux at the sediment–water interface, based on measured porewater Mn distributions (Table 2). Our diffusive Mn flux calculations must be interpreted with caution, as they are based on porewater Mn profiles with 3 mm resolution in surface sediments, and they may overestimate Mn flux due to Mn oxidation and precipitation at the sediment–water interface. Nevertheless, the Mn fluxes estimated in this study fall within the range of previously published fluxes in nearshore environments, from 0 to 0.2 mmol m^{-2} h^{-1} (Sundby and Silverberg, 1985; Aller, 1994; Thamdrup et al., 1994; Friedl et al., 1998; Warnken et al., 2001; Pakhomova et al., 2007). Ocean margin sediments act as a Mn source to the open ocean, as benthic Mn fluxes in shallow sediments are considerably higher than in deeper sediments

(Burdige, 1993; McManus et al., 2012) and dissolved and particulate river inputs (Bender et al., 1977). By remobilizing Mn adsorbed onto $CaCO_3$ and FeS minerals and enhancing diffusive Mn efflux in coastal sediments, e-SOx may accelerate margin sources of Mn to the open ocean.

4.6. Carbon and nutrient cycling

Electrogenic sulfide oxidation may play an important role in benthic carbon and nutrient cycling, as shown by a recent report that cable bacteria can couple sulfide oxidation to NO_3^- reduction in the absence of O_2 (Marzocchi et al., 2014). The intensification of Fe cycling by e-SOx likely induces additional effects on C and nutrient biogeochemistry.

An unexpected increase in organic C content was observed in the upper 5 cm of sediment in oxic cores over the course of this experiment, in parallel with the development of e-SOx (Figs. 5 and 6). To examine the potential origin of the accumulating organic material, we estimated the maximum increase in sediment organic C content due to cable bacteria growth. Assuming maximum cable bacteria density (2380 m of cables per cm^2 of sediment, Schauer et al., 2014), maximum filament width (2.4 μm; Malkin et al., 2014), a conversion from microbial biovolume to dry weight according to Loferer-Krößbacher et al. (1998), and a dry weight C content of 50%, we estimate an increase in sediment organic C content of 0.08 mol m^{-2} over the course of this experiment. As this is much smaller than the observed increase in sediment organic C content ($\sim$2.9 mol m^{-2}; Fig. 6), we conclude that cable bacteria growth could only be responsible for a very small fraction of the organic matter accumulation over the course of this experiment.

We hypothesize that much of the organic matter that accumulated during e-SOx development may be associated with reactive Fe in the developing Fe oxide crust (Figs. 5 and 6, Section 4.4). Although organic matter associated with reactive Fe was not quantified in this study, the overlap between increasing organic matter and reactive Fe content in surface sediments is striking (Figs. 5 and 6). Organic matter is known to be intimately linked with reactive Fe in soils and sediments (Lalonde et al., 2012; Riedel et al., 2013). High organic C:Fe molar ratios have been observed in a wide variety of continental margin sediments, and attributed to co-precipitation and/or chelation of organic compounds with Fe, permitting molar ratios greatly exceeding the maximum sorption capacity of Fe oxides (Lalonde et al., 2012). Authigenic reactive Fe oxides also promote the transfer of organic C from the dissolved to particulate phase, where they are more resistant to bacterial degradation, therefore favoring the preservation of organic matter in sediments (Barber et al., 2014).

Iron oxides also act as a reactive barrier to the release of remineralized phosphorus at the sediment–water interface due to PO_4^{3-} sorption and mineral formation (see review by Paytan and McLaughlin, 2007). Thus, the formation of an Fe oxide crust in surface sediments (Fig. 5) may suppress the release of remineralized P from sediments, as indicated by the sharp decline in PO_4^{3-} efflux from T0 to

T14 in the present study (Fig. 4 and Table 3). However, the immobilization of PO_4^{3-}, which is particularly evident in porewater profiles from T35, takes place throughout the upper 2 cm of sediments (Fig. 9), while the buildup of Fe oxides only occurs in the upper few mm's of sediments (Fig. 5). This discrepancy suggests an alternative or additional PO_4^{3-} sink associated with e-SOx development. One explanation is that cable bacteria may accumulate P internally, as in other sulfur oxidizing bacteria (Schulz et al., 1999). This is consistent with the vertical overlap between the thickness of the suboxic zone created by e-SOx (Table 1) and the zone of PO_4^{3-} immobilization in surface sediments at T35 (Fig. 9). Although more work is needed to elucidate the exact mechanism of P immobilization by cable bacteria, our data clearly shows that e-SOx activity reduces PO_4^{3-} efflux at the sediment–water interface.

A change from NO_3^- influx to NO_3^- efflux with time (Fig. 4) suggests an increase in nitrification in sediments from T0 to T71. Nitrification rates were likely stimulated by deeper O_2 penetration toward the end of the experiment (Table 1). Increased nitrification coupled with reduced ammonification in sediments (Fig. 9) may have induced the observed decline in NH_4^+ efflux over time (Fig. 4). A nitrogen mass balance based on the difference between N regeneration and DIN flux shows a small increase in N removal (N_r), coincident with e-SOx development (Table 3). While the increase in N_r is very small relative to the variability between replicate cores, this observation suggests that e-SOx may stimulate NO_3^- reduction in Grevelingen sediments, as observed previously by Marzocchi et al. (2014). More work is needed to investigate the significance of this NO_3^- reduction pathway in coastal sediments.

4.7. Alkalinity production in sediments

Alkalinity production in sediments was strongly intensified by e-SOx development, reaching a maximum at T14 and declining thereafter (Fig. 4 and Table 3). Based on the availability of carbonates in these sediments (Fig. 5), $CaCO_3$ dissolution was expected to represent an important source of TA, which we evaluate here based on the ratio of Ca^{2+} to TA efflux ($R_{Ca:TA}$, Table 3). This ratio should approach 0.5 if $CaCO_3$ dissolution is the dominant source of TA in sediments, and decrease as other TA sources become important. $R_{Ca:TA}$ was not significantly different from 0.5 at T0 (Student's t, 1-tailed: $t_2 = 3.00$, $p = 0.10$), T7 ($t_2 = -0.81$, $p = 0.50$), T35 ($t_2 = 0.52$, $p = 0.66$), and T71 ($t_2 = -1.34$, $p = 0.31$). These findings indicate that $CaCO_3$ dissolution ($CO_2 + H_2O + CaCO_3 \rightarrow Ca^{2+} + 2HCO_3^-$) was the principal TA source in these sediments. Measurements of $R_{Ca:TA}$ in one core each at T35 and T71 were anomalously high and low, respectively (Grubbs' test for 2 outliers on opposite tails, $G = 4.77$ with $n = 15$, $p < 0.001$). At the time of peak e-SOx activity and maximum TA flux (T14), $R_{Ca:TA}$ (0.36 ± 0.03) was significantly lower than 0.5 (Student's t, 1-tailed: $t_2 = -7.30$, $p < 0.01$), suggesting an important alternative TA source linked with e-SOx although a large part ($72 \pm 6\%$) of TA production was still due to net $CaCO_3$ dissolution.

Carbonate dissolution in the suboxic zone induced by the production of acidity associated with anodic sulfide oxidation resulted in the release of Ca^{2+} (Fig. 8), as shown in earlier studies (Risgaard-Petersen et al., 2012). The overlap between maximum $J_{current}$ and maximum Ca^{2+} efflux at T14 (Table 3 and Fig. 4) confirms that e-SOx is an important driver of $CaCO_3$ dissolution in Lake Grevelingen sediments. The stimulation of $CaCO_3$ dissolution in sediments by e-SOx represents a form of respiratory or metabolic dissolution (Archer, 1996), as it is driven by the production of metabolic acidity.

The remainder ($\sim$28%) of TA production at T14 cannot be explained by $CaCO_3$ dissolution but is clearly associated with e-SOx. The steep TA gradient that developed at the sediment–water interface by T14 (Fig. 8), concurrent with the rise in $J_{current}$ (Table 3), is consistent with proton consumption and TA production by cathodic O_2 reduction in surface sediments. Similarly, the removal of TA in the suboxic zone is consistent with proton production by anodic sulfide oxidation. Hence, the spatial decoupling of redox half-reactions by e-SOx, and the subsequent spatial decoupling of proton consumption and production results in an "alkalinity pump", whereby alkalinity is transferred from the suboxic zone to surface sediments at the base of the oxic zone. This "alkalinity pump" increases the vertical gradient in TA at the sediment–water interface and therefore accelerates TA flux into the overlying water (Figs. 4 and 8).

Whereas TA efflux was strongly stimulated by e-SOx development, R_{min} remained nearly constant for the duration of the experiment, resulting in a remarkable ($>4\times$) increase in the ratio of TA:DIC flux in sediments from T0 to T14 ($R_{TA:DIC}$, Table 3), and a subsequent decline from T14 to T71. These results further reveal a positive correlation between $R_{TA:DIC}$ and e-SOx activity (Pearson's $r_3 = 2.64$, $p = 0.04$), if one core with anomalously high $R_{TA:DIC}$ at T71 is omitted (Grubbs' test for one outlier, $G = 3.04$ with $n = 15$, $p < 0.001$). Based on this analysis, it appears that e-SOx can fundamentally alter benthic-pelagic coupling with respect to the carbonate system. By stimulating the release of TA to a greater extent than DIC at the sediment–water interface, e-SOx effectively buffers the acidification of seawater by benthic metabolism. Since this effect counteracts a pH decline in the overlying water due to the release of respiratory DIC, and maintains low pCO_2 in coastal waters, it has the potential to offset coastal ocean acidification and increase net CO_2 uptake from the atmosphere in coastal regions (Thomas et al., 2009). This effect is largely fueled by $CaCO_3$ dissolution associated with anodic sulfide oxidation, but a portion (about ¼) of the buffering effect of e-SOx on seawater pH is driven by the "alkalinity pump" described above.

In this study, $CaCO_3$ dissolution resulted in a decline in TIC content in subsurface sediments between 0.5 and 3 cm depth (Figs. 5 and 6). Previous studies have reported that high pH due to cathodic O_2 reduction and upward diffusion of Ca^{2+} from $CaCO_3$ dissolution at depth favored porewater supersaturation and precipitation of an authigenic high-Mg calcite cement in surface sediments (Risgaard-Petersen et al., 2012). However, no TIC enrichment was observed in surface sediments in the present experiment (Fig. 5).

TIC profiles varied in replicate cores but overall, the depth-integrated sediment TIC inventory appeared to decline following e-SOx development (Fig. 6), suggesting that dissolution was stronger than reprecipitation. TIC removal was not observed in control cores without e-SOx (Fig. 5), supporting the link between TIC reduction and e-SOx. These results suggest that e-SOx may reduce $CaCO_3$ preservation in coastal sediments, which are responsible for about one-half of the total $CaCO_3$ sediment accumulation in the world's oceans (Milliman and Droxler, 1996). In this way, e-SOx may accelerate the buffering of coastal ocean pH by enhancing $CaCO_3$ dissolution in sediments.

In Den Osse basin, the effect of e-SOx on TA production in sediments may contribute to a rise in bottom water pH, alkalinity, benthic proton consumption, and atmospheric CO_2 uptake in spring (Hagens et al., 2015), coincident with a peak in cable bacteria density (Seitaj et al., 2014). With the onset of water column stratification in summer, benthic respiration induces strong bottom water hypoxia and acidification (Hagens et al., 2015), and cable bacteria densities decline (Seitaj et al., 2014). While the influence of e-SOx on water column pH and air-sea CO_2 exchange in Lake Grevelingen was not tested quantitatively, we hypothesize that this process may influence the seasonal variability in the CO_2 system observed at this site.

5. CONCLUSIONS

In this study, we investigated the influence of electrogenic sulfur oxidation by cable bacteria on biogeochemical cycling and benthic-pelagic coupling in coastal sediment. The rise and fall in e-SOx was accompanied by an increase and subsequent decline in total O_2 consumption in sediments. Ferrous iron was remobilized by FeS dissolution fueled by anodic sulfide oxidation. Dissolved Fe diffusing downward was reprecipitated as FeS, and upward diffusing Fe_d was reoxidized in surface sediments, forming a surface crust of amorphous Fe oxides. These observations confirm that e-SOx strengthens benthic Fe turnover, and we hypothesize that cyclical variability in e-SOx activity may activate a switch from periods of FeS accumulation to periods of FeS removal in sediments. Diffusive Mn release was also stimulated by e-SOx, likely due to the release of adsorbed Mn from FeS and/or $CaCO_3$ surfaces, as these minerals dissolve in the suboxic zone due to the production of acidity by anodic sulfide oxidation. Reactive Fe precipitation in surface sediments led to enhanced organic matter accumulation and reduced interfacial PO_4^{3-} efflux. Overall, our findings show that e-SOx has the potential to promote organic matter preservation in coastal sediments and fundamentally alter benthic-pelagic coupling with respect to nutrients, metals, and organic carbon.

The development of e-SOx resulted in a ninefold increase in interfacial alkalinity flux, which was attributed to two mechanisms of TA production. The majority ($72 \pm 6\%$) of TA release associated with e-SOx was attributed to $CaCO_3$ dissolution, while the remainder ($28 \pm 6\%$) was attributed to an alkalinity pump induced by e-SOx, transferring TA removed from deeper suboxic sediments by anodic sulfide oxidation (an alkalinity sink) to cathodic

O_2 consumption (an alkalinity source) in oxic surface sediments. This upward alkalinity pump increases the TA gradient at the sediment–water interface and its exchange with the overlying water. Our results show that e-SOx may reduce TIC preservation in coastal sediments, offset coastal ocean acidification and enhance atmospheric CO_2 uptake in coastal regions by stimulating the release of TA relative to DIC in sediments.

REFERENCES

Aller R. C. (1994) The sedimentary Mn cycle in Long Island Sound: its role as intermediate oxidant and the influence of bioturbation, O_2, and C_{org} flux on diagenetic reaction balances. *J. Mar. Res.* **52**, 259–295.

Arakaki T. and Morse J. W. (1993) Coprecipitation and adsorption of Mn(II) with mackinawite (FeS) under conditions similar to those found in anoxic sediments. *Geochim. Cosmochim. Acta* **57**, 9–14.

Archer D. (1996) A data-driven model of the global calcite lysocline. *Global Biogeochem. Cycles* **10**, 511–526.

Barber A., Lalonde K., Mucci A. and Gélinas Y. (2014) The role of iron in the diagenesis of organic carbon and nitrogen in sediments: a long-term incubation experiment. *Mar. Chem.* **162**, 1–9.

Bender M. L., Klinkhammer G. P. and Spencer D. W. (1977) Manganese in seawater and the marine manganese balance. *Deep Sea Res.* **24**, 799–812.

Berelson W. M., Townsend T., Heggie D., Ford P., Longmore A., Skyring G., Kilgore T. and Nicholson G. (1999) Modelling bio-irrigation rates in the sediments of Port Phillip Bay. *Mar. Freshwater Res.* **50**, 573–579.

Berg P., Risgaard-Petersen N. and Rysgaard S. (1998) Interpretation of measured concentration profiles in sediment pore water. *Limnol. Oceanogr.* **43**, 1500–1510.

Boudreau B. P. (1997) *Diagenetic Models and Their Implementation: Modelling Transport and Reactions in Aquatic Sediments*. Springer, New York.

Brewer P. G. and Spencer D. W. (1971) Colorimetric determination of manganese in anoxic waters. *Limnol. Oceanogr.* **16**, 107–110.

Burdige D. (1993) The biogeochemistry of manganese and iron reduction in marine sediments. *Earth-Sci. Rev.* **35**, 249–284.

Canfield D. E., Thamdrup B. and Hansen J. W. (1993) The anaerobic degradation of organic matter in Danish coastal sediments: iron reduction, manganese reduction, and sulfate reduction. *Geochim. Cosmochim. Acta* **57**, 3867–3883.

Cline J. D. (1969) Spectrophotometric determination of hydrogen sulfide in natural waters. *Limnol. Oceanogr.* **14**, 454–458.

Cornwell J. C. and Morse J. W. (1987) The characterization of iron sulfide minerals in anoxic marine sediments. *Mar. Chem.* **22**, 193–206.

Cyronak T., Santos I. R., Erler D. V. and Eyre B. D. (2013a) Groundwater and porewater as major sources of alkalinity to a fringing coral reef lagoon (Muri Lagoon, Cook Islands). *Biogeosciences* **10**, 2467–2480.

Cyronak T., Santos I. R., McMahon A. and Eyre B. D. (2013b) Carbon cycling hysteresis in permeable carbonate sands over a diel cycle: implications for ocean acidification. *Limnol. Oceanogr.* **58**, 131–143.

Damgaard L. R., Risgaard-Petersen N. and Nielsen L. P. (2014) Electric potential microelectrode for studies of electrobiogeophysics. *J. Geophys. Res. G: Biogeosci.* **119**, 1906–1917.

Dickson A. G. (1990) Standard potential of the reaction: AgCl(s) + 1/2H$_2$(g) = Ag(s) + HCl(aq), and the standard acidity constant of the ion HSO$_4$ in synthetic sea water from 273.15 to 318.15 K. *J. Chem. Thermodyn.* **22**, 113–127.

Dickson A. G., Afghan J. D. and Anderson G. C. (2003) Reference materials for oceanic CO$_2$ analysis: a method for the certification of total alkalinity. *Mar. Chem.* **80**, 185–197.

Dickson A. G., Sabine C. L. and Christian J. R. (2007) Guide to best practices for ocean CO$_2$ measurements. *PICES Spec. Publ.* **3**, 191.

Faber P. A., Kessler A. J., Bull J. K., McKelvie I. D., Meysman F. J. R. and Cook P. L. M. (2012) The role of alkalinity generation in controlling the fluxes of CO$_2$ during exposure and inundation on tidal flats. *Biogeosciences* **9**, 4087–4097.

Franklin M. L. and Morse J. W. (1983) The interaction of manganese(II) with the surface of calcite in dilute solutions and seawater. *Mar. Chem.* **12**, 241–254.

Friedl G., Dinkel C. and Wehrli B. (1998) Benthic fluxes of nutrients in the northwestern Black Sea. *Mar. Chem.* **62**, 77–88.

Gebhardt A., Petzoldt T. and Maechler M. (2009) AKIMA: Interpolation of irregularly spaced data. *R package version 0.5-4 Software.*

Giblin A. E., Weston N. B., Banta G. T., Tucker J. and Hopkinson C. S. (2010) The effects of salinity on nitrogen losses from an oligohaline estuarine sediment. *Estuaries Coasts* **33**, 1054–1068.

Gribsholt B. and Kristensen E. (2003) Benthic metabolism and sulfur cycling along an inundation gradient in a tidal *Spartina anglica* salt marsh. *Limnol. Oceanogr.* **48**, 2151–2162.

Hagens M., Slomp C. P., Meysman F. J. R., Seitaj D., Harlay J., Borges A. V. and Middelburg J. J. (2015) Biogeochemical processes and buffering capacity concurrently affect acidification in a seasonally hypoxic coastal marine basin. *Biogeosciences* **12**, 1561–1583.

Heip C., Goosen N. K., Herman P. M. J., Kromkamp J., Middelburg J. J. and Soetaert K. (1995) Production and consumption of biological particles in temperate tidal estuaries. *Oceanogr. Mar. Biol.* **33**, 1–149.

Hofmann A. F., Soetaert K., Middelburg J. J. and Meysman F. J. R. (2010) AquaEnv: an aquatic acid-base modelling environment in R. *Aquat. Geochem.* **16**, 507–546.

Hu X. and Cai W.-J. (2011) An assessment of ocean margin anaerobic processes on oceanic alkalinity budget. *Global Biogeochem. Cycles* **25**, GB3003.

Jahnke R. A. and Jahnke D. B. (2000) Rates of C, N, P and Si recycling and denitrification at the US Mid-Atlantic continental slope depocenter. *Deep Sea Res. I* **47**, 1405–1428.

Kallmeyer J., Ferdelman T. G., Weber A., Fossing H. and Jørgensen B. B. (2004) A cold chromium distillation procedure for radiolabeled sulfide applied to sulfate reduction measurements. *Limnol. Oceanogr. Meth.* **2**, 171–180.

Kelderman P., Nieuwenhuize J., Meerman-van de Repe A. M. and Van Liere J. M. (1984) Changes of sediment distribution patterns in Lake Grevelingen, an enclosed estuary in the SW Netherlands. *Neth. J. Sea Res.* **18**, 273–285.

Kostka J. E. and Luther G. W. (1994) Partitioning and speciation of solid phase iron in saltmarsh sediments. *Geochim. Cosmochim. Acta* **58**, 1701–1710.

Lalonde K., Mucci A., Ouellet A. and Gelinas Y. (2012) Preservation of organic matter in sediments promoted by iron. *Nature* **483**, 198–200.

Lavigne H., Epitalon J. -M. and Gattuso J. -P. (2011) SEACARB: Seawater carbonate chemistry with R. *R package version 3.0 Software.*

Loferer-Krößbacher M., Klima J. and Psenner R. (1998) Determination of bacterial cell dry mass by transmission electron microscopy and densitometric image analysis. *Appl. Environ. Microbiol.* **64**, 688–694.

Lueker T. J., Dickson A. G. and Keeling C. D. (2000) Ocean pCO2 calculated from dissolved inorganic carbon, alkalinity, and equations for K1 and K2: validation based on laboratory measurements of CO$_2$ in gas and seawater at equilibrium. *Mar. Chem.* **70**, 105–119.

Madison A. S., Tebo B. M., Mucci A., Sundby B. and Luther, 3rd, G. W. (2013) Abundant porewater Mn(III) is a major component of the sedimentary redox system. *Science* **341**, 875–878.

Malkin S. Y., Rao A. M., Seitaj D., Vasquez-Cardenas D., Zetsche E. M., Hidalgo-Martinez S., Boschker H. T. and Meysman F. J. (2014) Natural occurrence of microbial sulphur oxidation by long-range electron transport in the seafloor. *ISME J.* **8**, 1843–1854.

Manz W., Amann R., Ludwig W., Wagner M. and Schleifer K.-H. (1992) Phylogenetic oligodeoxynucleotide probes for the major subclasses of proteobacteria: problems and solutions. *Syst. Appl. Microbiol.* **15**, 593–600.

Martin J. H. and Knauer G. A. (1984) VERTEX: manganese transport through oxygen minima. *Earth Planet. Sci. Lett.* **67**, 35–47.

Marzocchi U., Trojan D., Larsen S., Meyer R. L., Revsbech N. P., Schramm A., Nielsen L. P. and Risgaard-Petersen N. (2014) Electric coupling between distant nitrate reduction and sulfide oxidation in marine sediment. *ISME J.* **8**, 1682–1690.

McManus J., Berelson W. M., Severmann S., Johnson K. S., Hammond D. E., Roy M. and Coale K. H. (2012) Benthic manganese fluxes along the Oregon-California continental shelf and slope. *Cont. Shelf Res.* **43**, 71–85.

Merks A. G. A. and Sinke J. J. (1981) Application of an automated method for dissolved sulphate analysis to marine and brackish waters. *Mar. Chem.* **10**, 103–108.

Meysman F. J. R., Risgaard-Petersen N., Malkin S. Y. and Nielsen L. P. (2015) The geochemical fingerprint of microbial long-distance electron transport in the seafloor. *Geochim. Cosmochim. Acta* **152**, 122–142.

Middelburg J. J., de Lange G. and van der Weijden C. H. (1987) Manganese solubility control in marine pore waters. *Geochim. Cosmochim. Acta* **51**, 759–763.

Millero F. J. (1995) Thermodynamics of the carbon dioxide system in the oceans. *Geochim. Cosmochim. Acta* **59**, 661–677.

Milliman J. D. and Droxler A. W. (1996) Neritic and pelagic carbonate sedimentation in the marine environment: ignorance is not bliss. *Geol. Rundsch.* **85**, 496–504.

Mucci A. (2004) The behavior of mixed Ca–Mn carbonates in water and seawater: controls of manganese concentrations in marine porewaters. *Aquat. Geochem.* **10**, 139–169.

Nielsen L. P., Risgaard-Petersen N., Fossing H., Christensen P. B. and Sayama M. (2010) Electric currents couple spatially separated biogeochemical processes in marine sediment. *Nature* **463**, 1071–1074.

Pakhomova S. V., Hall P. O. J., Kononets M. Y., Rozanov A. G., Tengberg A. and Vershinin A. V. (2007) Fluxes of iron and manganese across the sediment–water interface under various redox conditions. *Mar. Chem.* **107**, 319–331.

Paytan A. and McLaughlin K. (2007) The oceanic phosphorus cycle. *Chem. Rev.* **107**, 563–576.

Perez F. F. and Fraga F. (1987) Association constant of fluoride and hydrogen ions in seawater. *Mar. Chem.* **21**, 161–168.

Pfeffer C., Larsen S., Song J., Dong M., Besenbacher F., Meyer R. L., Kjeldsen K. U., Schreiber L., Gorby Y. A., El-Naggar M. Y., Leung K. M., Schramm A., Risgaard-Petersen N. and Nielsen L. P. (2012) Filamentous bacteria transport electrons over centimetre distances. *Nature* **491**, 218–221.

Presley B. J. (1971) Techniques for analyzing interstitial water samples. Part I. Determination of selected minor and major inorganic constituents. In *Initial Reports of the Deep Sea Drilling Project* (eds. E. L. R. Winterer, W. R. Riedel, P. Brönnimann, E. Gealy, G. Heath, L. Kroenke, E. Martini, , Jr. R. Moberly, J. Resig and T. Worsley). U.S. Government Printing Office, pp. 1749–1755.

Rao A. M., Malkin S. Y., Montserrat F. and Meysman F. J. (2014) Alkalinity production in intertidal sands intensified by lugworm bioirrigation. *Estuarine Coastal Shelf Sci.* **148**, 36–47.

Rao A. M. F., Polerecky L., Ionescu D., Meysman F. J. R. and de Beer D. (2012) The influence of pore-water advection, benthic photosynthesis, and respiration on calcium carbonate dynamics in reef sands. *Limnol. Oceanogr.* **57**, 809–825.

Riedel T., Zak D., Biester H. and Dittmar T. (2013) Iron traps terrestrially derived dissolved organic matter at redox interfaces. *Proc. Natl. Acad. Sci. U.S.A.* **110**, 10101–10105.

Risgaard-Petersen N., Damgaard L. R., Revil A. and Nielsen L. P. (2014) Mapping electron sources and sinks in a marine biogeobattery. *J. Geophys. Res. Biogeosci.* **119**, 2014JG002673.

Risgaard-Petersen N., Revil A., Meister P. and Nielsen L. P. (2012) Sulfur, iron-, and calcium cycling associated with natural electric currents running through marine sediment. *Geochim. Cosmochim. Acta* **92**, 1–13.

Schauer R., Risgaard-Petersen N., Kjeldsen K. U., Tataru Bjerg J. J., Tataru Bjerg J. J., Jørgensen Bo B., Schramm A. and Nielsen L. P. (2014) Succession of cable bacteria and electric currents in marine sediment. *ISME J.* **8**, 1314–1322.

Schulz H. N., Brinkhoff T., Ferdelman T. G., Mariné M. H., Teske A. and Jørgensen B. B. (1999) Dense populations of a giant sulfur bacterium in Namibian shelf sediments. *Science* **284**, 493–495.

Seitaj D., Malkin S. Y., Schauer R. and Meysman F. J. (2014) Microbial sulphide oxidation in seasonally hypoxic coastal sediments: competition between electrogenic filamentous bacteria and Beggiatoa. *Ocean Sciences Meeting*. Honolulu, USA.

Seitzinger S. P., Nixon S. and Pilson M. E. Q. (1984) Denitrification and nitrous oxide production in a coastal marine ecosystem. *Limnol. Oceanogr.* **29**, 73–83.

Soetaert K., Petzoldt T. and Meysman F. J. R. (2010) MARELAC: tools for aquatic science. *R package version 2.1.2 Software*.

Sundby B. and Silverberg N. (1985) Manganese fluxes in the benthic boundary layer. *Limnol. Oceanogr.* **30**, 372–381.

Thamdrup B. and Canfield D. E. (1996) Pathways of carbon oxidation in continental margin sediments off central Chile. *Limnol. Oceanogr.* **41**, 1629–1650.

Thamdrup B., Fossing H. and Jørgensen B. B. (1994) Manganese, iron and sulfur cycling in a coastal marine sediment, Aarhus bay, Denmark. *Geochim. Cosmochim. Acta* **58**, 5115–5129.

Thomas H., Schiettecatte L.-S., Suykens K., Koné Y. J. M., Shadwick E. H., Prowe A. E. F., Bozec Y., de Baar H. J. W. and Borges A. V. (2009) Enhanced ocean carbon storage from anaerobic alkalinity generation in coastal sediments. *Biogeosciences* **6**, 267–274.

Tsunogai S., Nishimura M. and Nakaya S. (1968) Complexometric titration of calcium in the presence of larger amounts of magnesium. *Talanta* **15**, 385–390.

Vasquez-Cardenas D., van de Vossenberg J., Polerecky L., Malkin S. Y., Schauer R., Hidalgo-Martinez S., Confurius V., Middelburg J. J., Meysman F. J. and Boschker H. T. (2015) Microbial carbon metabolism associated with electrogenic sulphur oxidation in coastal sediments. *ISME J.*

Viollier E., Inglett P. W., Hunter K., Roychoudhury A. N. and Van Cappellen P. (2000) The ferrozine method revisited: Fe(II)/Fe(III) determination in natural waters. *Appl. Geochem.* **15**, 785–790.

Warnken K. W., Gill G. A., Griffin L. L. and Santschi P. H. (2001) Sediment-water exchange of Mn, Fe, Ni and Zn in Galveston Bay, Texas. *Mar. Chem.* **73**, 215–231.

Associate editor: Orit Sivan